

Interaction and coherence in two-dimensional bilayersJihang Zhu  and Sankar Das Sarma*Condensed Matter Theory Center and Joint Quantum Institute, Department of Physics, University of Maryland, College Park, Maryland 20742, USA*

(Received 17 December 2023; accepted 5 February 2024; published 20 February 2024)

Two-dimensional electron gas (2DEG) bilayers provide suitable platforms for electronic phases and transitions that are fundamental to both theoretical physics and practical applications in device technology. In bilayer systems, the additional pseudospin, representing the layer degree of freedom, enables the emergence of interlayer coherence, which is a direct consequence of the interlayer Coulomb interaction. This study presents a comprehensive Hartree-Fock (HF) mean-field investigation of the interlayer coherence in 2D bilayers, uncovering ground-state behaviors and temperature-dependent phase transitions that are distinct from single-layer 2DEG. This interlayer coherence signals a spontaneous breaking of the $U(1)$ symmetry in layer pseudospin. We explore the zero-temperature phase diagrams as a function of the electron density and interlayer separation within the HF formalism. We also calculate the critical temperature (T_c) of the interlayer coherence onset by self-consistently solving the HF gaplike equation. We contrast this interlayer coherent phase in electron-electron (e-e) bilayers with the closely related excitonic superfluid phase in electron-hole (e-h) bilayers. Although both e-e and e-h bilayers spontaneously break the pseudospin $U(1)$ symmetry, e-h bilayers produce Bardeen-Cooper-Schrieffer-Bose-Einstein condensates crossover intrinsic to the excitons acting as effective bosons or Cooper pairs, whereas the symmetry-broken phase in e-e bilayers is akin to the XY or easy-plane pseudospin ferromagnetism. Using the same system parameters and a similar theoretical framework, we find that T_c of the interlayer coherent phase in e-e bilayers is about one-third of that in exciton condensates, suggesting a weaker interlayer coherence in e-e bilayers. In addition, we examine the effect of a weak interlayer tunneling on the interlayer coherence order parameter, drawing parallels with the influence of an effective in-plane magnetic field on the XY pseudospin ferromagnetism. Our findings provide a comparative theoretical framework that bridges the gap between the interlayer coherence physics in e-e and e-h bilayers, contributing to a unified understanding of phase transitions in low-dimensional electron-hole systems and establishing in particular the same universality class for interlayer phase coherence in both e-e and e-h bilayers.

DOI: [10.1103/PhysRevB.109.085129](https://doi.org/10.1103/PhysRevB.109.085129)**I. INTRODUCTION**

During the last 50 years, the fabrication and exploration of two-dimensional electron gas (2DEG) systems has been crucial in expanding our understanding of quantum mechanical phenomena in condensed matter physics [1,2]. These systems, fundamental to the functionality of contemporary electronic devices such as Si MOSFETs and GaAs HEMTs, exhibit rich many-body quantum phases under various conditions, for example, at low electron densities or in a strong magnetic field where Coulomb interactions dominate. The most famous such interacting phase is the fractional quantum Hall effect [2], but many other correlation-induced phases, both in finite and zero magnetic fields, have been predicted and sometimes observed, such as the Wigner crystal [3], the Bloch ferromagnet [4], spin/valley/charge density waves, etc.

The Bardeen-Cooper-Schrieffer (BCS) theory [5,6] describes the pairing of two electrons into a Cooper pair as a result of effective attraction mediated by phonons. An analogous pairing mechanism, induced directly by the Coulomb interaction, arises between an electron and a hole, giving rise to the excitonic state in semimetals or semiconductors [7–11]. Even though the original concept of an exciton [12–14] describes the bound state of an electron and a hole, which

are generated optically in the conduction and valence bands of homogeneous semiconductors, this kind of exciton is an excited state. Excitons formed in e-h bilayers are, however, the ground state of the bilayer system. We only consider such electron-hole (e-h) bilayer excitons and the corresponding excitonic ground states in this work. The nature of these excitonic states is determined by the pairing strength. In the weak pairing limit, excitons are loosely bound with radii larger than the average distance between electrons and holes. In this regime, the original semimetallic or semiconducting phase is unstable for an arbitrarily weak e-h attraction, akin to how the normal Fermi surface of a metal is susceptible to the Cooper-pair formation under any weak e-e attraction in the BCS theory. In the strong pairing limit, where excitons are tightly bound with smaller radii, excitons behave like a weakly repulsive dilute Bose gas, forming the Bose-Einstein condensates (BEC) at low temperatures. In either limit, as long as the electrons and holes remain spatially separated, excitons condense into a ground state which is a BCS or BEC superfluid. Such a superfluid is not a regular superconductor since excitons are electrically neutral, thus, this ground state is sometimes called the “excitonic insulator.” It also differs from a regular insulator since this excitonic ground state constitutes a neutral superfluid. We use the terminology “exciton

condensates” for the $T = 0$ strongly bound BEC or weakly bound BCS superfluid of 2D e-h bilayer excitons.

Advances in quantum well bilayers, such as InAs-GaSb [15] and GaAs-AlGaAs [16–18] heterostructures, have enabled the spatial separation of electrons and holes, and therefore the creation of more stable and controllable e-h bilayers. These developments have facilitated the observations of stable excitonic states in equilibrium [15,19–26]. In these quantum well bilayers, particularly, exciton condensation has been predicted and observed in a strong magnetic field perpendicular to the 2D layers [27–33]. The most stable exciton condensates manifest at a total Landau-level filling factor of $\nu = 1$, where each layer’s lowest Landau level is half-filled. The emergence of these exciton condensates has been further reinforced by recent breakthroughs in 2D material fabrications [34,35], including double-layer graphene [36,37], double-bilayer graphene, and double-layer transition metal dichalcogenides. Graphene double layers [37], in particular, have demonstrated the potential for a BCS–BEC crossover [15,38–49], a continuum between BCS-type weak coupling and BEC-type strong coupling regimes, in condensed matter systems.

In contrast to quantum Hall bilayers, exciton condensates in e-h bilayers without an external magnetic field, hereafter simply referred to as e-h bilayers, have remained elusive [15] until the recent observation of enhanced interlayer tunneling anomaly in double-bilayer graphene heterostructures [50], signaling the first indication of such condensates. Considerable obstacles in experimental realization of e-h bilayer exciton condensates have been the difficulties in eliminating impurities and in approaching the BEC limit. The latter involves electrostatically doping carriers to a lower density, minimizing interlayer tunneling and simultaneously reducing the distance between layers. Regardless of the specific pairing mechanism, these bilayer systems, with or without an external magnetic field, doped with electrons or holes, share a common core: the spontaneous interlayer coherence associated with an excitonic superfluid arising from Coulomb interactions.

The relative stability of exciton BEC in quantum Hall bilayers at $\nu = 1$ can be attributed to the unique characteristics of Landau levels. Electrons in Landau levels bypass the cost of kinetic energies, thus enhancing interaction-dominated symmetry-broken phases. Furthermore, the quantum Hall bilayer is distinguished by the exact particle-hole symmetry inherent in the Landau level around the half-filling. At $\nu = 1$, despite both layers being electron-doped and half-filling the lowest Landau level, the exact particle-hole symmetry transforms electrons into holes, and vice versa: quantum Hall bilayers at $\nu = 1$ can be equivalently considered as e-e, h-h, or e-h bilayers, and thus equivalently describable as an XY pseudospin ferromagnet in the e-e or h-h picture [51–59] or as a BEC superfluid in the e-h picture [29,33]. However, the absence of exact particle-hole symmetry, due to differing energy dispersions of electrons and holes, in e-h bilayers prevents a direct mapping between BEC and pseudospin ferromagnetism. This naturally raises an essential question: How do the nature and characteristics of interlayer coherence differ between e-h and e-e bilayers at zero magnetic field? Are they the same or different in the absence of particle-hole symmetry? In this paper, we address this question in depth using

the Hartree-Fock (HF) mean-field theory, which has also been used extensively to study the quantum Hall bilayer exciton condensation phenomena.

Although the comparison between BCS superconductivity and exciton condensates has a long history, there has been no in-depth discussion comparing the pairings in e-h and e-e bilayers. Closely related, e-e and e-h bilayers both host spontaneous interlayer coherence as a result of repulsive Coulomb interactions between electrons (or attraction between electrons and holes). In spite of the same Coulombic nature, the interlayer coherence in these two systems exhibits distinct properties. In e-h bilayers, the formation of exciton condensates features a gap opening, while the interlayer coherence in e-e bilayers is more akin to an XY pseudospin ferromagnetism [60]. As previously discussed in depth in Refs. [61,62], the layer index introduces a pseudospin, of which the z component maps to the classical layer index. The pseudospin-ordered state underscores the quantum mechanical subtleties of pseudospin-orientation-dependent energies: the XY easy-plane pseudospin ferromagnetic state is energetically favorable due to the absence of Hartree contribution. A profound distinction arises between the symmetry properties of spin and pseudospin. Whereas conventional spin system exhibits SU(2) symmetry, ensuring energy invariance under any rotation of spin orientation, the symmetry of the pseudospin-ordered state in bilayer systems is reduced to U(1) [63,64] which only guarantees energy invariance under rotations in the plane perpendicular to the effective magnetic field. This reduction in symmetry from SU(2) to U(1) reflects the underlying order imposed by the difference between the intralayer and interlayer Coulomb interactions, which is unique to the bilayer systems. This pseudospin U(1) symmetry captures the essence of interlayer coherence, akin to the phase coherence in BCS superconductors.

In this work we focus on the zero-field e-e bilayers, which have been much less studied than the corresponding well-studied e-h bilayers although both manifest similar U(1) symmetry breaking associated with spontaneous interlayer coherence, which physically implies the system developing interaction-induced interlayer tunneling in spite of the absence of any single-particle interlayer tunneling. Specifically, we consider a bilayer structure, composed of two 2DEG layers confined in the xy plane and separated by a distance d in the z direction. Such a bilayer structure introduces new physics [65]: in addition to 2D carrier density in each layer, controlling the kinetic energy and the intralayer interaction strength, the layer separation provides a length and interaction scale for interlayer correlations. We study the interlayer coherence in such an e-e bilayer using the HF theory and, for completeness, we compare its finite-temperature properties with e-h bilayers using the same system parameters. We pedagogically start in Sec. II by introducing four distinct ground-state *Ansätze*: the spin and pseudospin unpolarized phase S_0 , the spin-polarized but pseudospin unpolarized phase S_1 , the spin-polarized and interlayer coherent phase with pseudospin in the xy plane S_2 , and the spin-polarized and interlayer coherent phase with pseudospin in z direction S_3 . We focus exclusively on the spin-polarized case in interlayer coherent phases, primarily because spin plays no role in the XY pseudospin ferromagnetic state if the density is lower than the critical value of the

ferromagnetic instability ($r_s > 2$) and the spin-orbit coupling is absent: the system is effectively spinless. Therefore, our findings regarding the interlayer coherence remain equally applicable to spinless itinerant electrons, with the only difference being the absence of spin polarization in each layer. The fact that a 2DEG has an exchange-driven spin-polarization transition at low density (for $r_s \sim 2$) [4] is well known, and our spin-polarization transition results are for the sake of completeness only.

In Sec. III, we study the interplay of kinetic, Hartree, and exchange energies, by mapping out the zero-temperature phase diagrams as a function of electron density and interlayer separation. We partition the discussion into two subsections to consider scenarios of equal layer densities (Sec. III B) and unequal layer densities (Sec. III C), both conditions being experimentally adjustable through the application of dual gate voltages. Interestingly, within the S_1 and S_2 regimes in the HF energy landscape, our findings suggest a ground state that favors a pseudospin partially polarized phase: both pseudospin up and pseudospin down are, unequally, occupied. This contrasts with a fully polarized phase where pseudospin alignment would be exclusively in the x direction [actually any direction in the xy plane because of the $U(1)$ symmetry].

In Sec. IV, we extend our study to finite temperatures, focusing on bilayers with equal layer densities. We provide an in-depth investigation of the critical temperature T_c for the interlayer coherent phase (S_2) in Sec. IV A, drawing comparisons to the exciton condensation in e-h bilayers with the same system parameters in Sec. IV B. The trends of T_c , as a function of density and interlayer separation, of e-e bilayers qualitatively deviate from that of e-h bilayers. The magnitude of T_c , on the other hand, in e-e bilayers is approximately one-third of that in e-h bilayers, suggesting a weaker interlayer coherence in e-e bilayers. Both the XY ferromagnetism and the exciton condensates undergo, in principle, a finite-temperature Berezinskii-Kosterlitz-Thouless (BKT) transition, and belong to the same universality class of phase transitions.

Section V investigates the influence of a weak interlayer tunneling on the interlayer coherence order parameter. The presence of any finite interlayer single-particle tunneling explicitly breaks the $U(1)$ symmetry and pins the easy-plane pseudospin ferromagnetism along the x direction. This analysis provides insights into the phase coherence and stability under perturbations that mimic the influence of an external magnetic field to physical spins.

Finally, we conclude with a discussion in Sec. VI. We comment on possible experimental signatures of the interlayer coherence in e-e bilayers and limitations of the HF mean-field theory.

In addition, we provide in Appendix A some useful summations and integrals that are used in our theory, in Appendix B the HF energy plots of the four competing ground states S_0, S_1, S_2, S_3 , and in Appendix C the T_c of the spin-polarized phases in single 2DEG and three-dimensional electron gas (3DEG) systems for completeness.

II. GROUND-STATE ANSATZ

We start from the characterization of four distinct ground states that emerge in the study of interlayer coherence in e-e

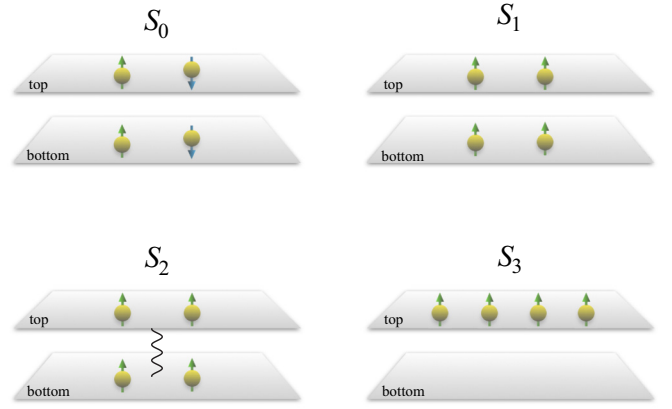


FIG. 1. Schematically shows the four competing ground states we consider: the spin- and pseudospin-unpolarized phase S_0 , the spin-polarized but pseudospin-unpolarized phase S_1 , the spin-polarized interlayer coherent (pseudospin-polarized) phase with the pseudospin in the xy plane S_2 (the XY order) and with the pseudospin in the z direction S_3 (the Ising order). In the S_3 phase, all electrons spontaneously move to one layer creating a charge order. The interlayer coherence is indicated by the wiggles. (The S_ξ phase mentioned in the main text consists of both S_2 and S_3 phases.)

(or h-h) bilayers. We designate these states with concise labels for ease of reference throughout our discussion:

- (i) S_0 phase: the spin- and pseudospin-unpolarized state.
- (ii) S_1 phase: the spin-polarized but pseudospin-unpolarized state.
- (iii) S_ξ phase: the spin-polarized interlayer coherent (pseudospin-polarized) states; the pseudospin polarization in these states can be oriented differently:
 - (a) S_2 phase: the pseudospin is oriented within the xy plane (the XY order).
 - (b) S_3 phase: the pseudospin is oriented in the z direction (the Ising order).

S_2 and S_3 phases both break the $U(1)$ layer symmetry and correspond to SP-SY and SP-MO phases in Refs. [61,62], respectively. Figure 1 schematically illustrates these four competing ground states.

III. ZERO-TEMPERATURE PHASE DIAGRAMS

In this section, we provide zero-temperature phase diagrams of e-e bilayers. We first show the HF Hamiltonian and the formula of HF total energy, followed by explicit HF energy expressions of S_0, S_1, S_2 , and S_3 phases in Sec. III A. We then present phase diagrams with respect to electron density (or dimensionless interelectron distance r_s) and interlayer separation d for equal layer densities [61,62] in Sec. III B and for unequal layer densities in Sec. III C.

The Hamiltonian of a 2D bilayer consists of the kinetic part $\hat{\mathcal{H}}_0$ and the Coulomb interacting part $\hat{\mathcal{V}}$:

$$\hat{\mathcal{H}} = \hat{\mathcal{H}}_0 + \hat{\mathcal{V}}. \quad (1)$$

Represented in the second quantization form,

$$\hat{\mathcal{H}}_0 = \sum_{\mathbf{k}, l, \sigma} \varepsilon_{0,l}(\mathbf{k}) c_{l\sigma\mathbf{k}}^\dagger c_{l\sigma\mathbf{k}}, \quad (2)$$

where $l = t, b$ label top and bottom layers and $\sigma = \uparrow, \downarrow$ label spins. For free-electron gases, $\varepsilon_{0,l}(\mathbf{k}) = \hbar^2 k^2 / 2m_l^*$, and m_l^* is the effective mass. For simplicity, we assume $m_t^* = m_b^* = m^*$ throughout the rest of the paper. It is straightforward to generalize the case to unequal effective masses $m_t^* \neq m_b^*$, which will only quantitatively change the results we present in this paper. The interacting part is

$$\hat{V} = \frac{1}{2A} \sum_{\substack{\mathbf{k}, \mathbf{k}', \mathbf{q} \\ l, l', \sigma, \sigma'}} V_{\mathbf{q}}^{ll'} c_{l\sigma, \mathbf{k}+\mathbf{q}}^\dagger c_{l'\sigma', \mathbf{k}'-\mathbf{q}}^\dagger c_{l'\sigma', \mathbf{k}'} c_{l\sigma, \mathbf{k}}, \quad (3)$$

where $A = A_t = A_b$ is the system area. The 2D Coulomb potentials are different for the electrons in the same layer and

in different layers,

$$V_{\mathbf{q}}^{ll'} = V_{\mathbf{q}}^S \delta_{ll'} + V_{\mathbf{q}}^D (1 - \delta_{ll'}), \quad (4)$$

where

$$V_{\mathbf{q}}^S = \frac{2\pi e^2}{\epsilon q}, \quad V_{\mathbf{q}}^D = \frac{2\pi e^2}{\epsilon q} e^{-qd}, \quad (5)$$

d is the layer separation, and ϵ is the averaged dielectric constant of the surrounding medium. We note that the interaction is spin independent [i.e., SU(2) symmetric], but layer dependent [i.e., U(1) symmetric in pseudospin layer index].

The HF mean-field form of the interacting part \hat{V} is

$$\hat{V}_{\text{HF}} = \sum_{\mathbf{k}, l, \sigma} [(V_{H,l} + V_{x,l}^{\sigma\sigma}(\mathbf{k})) c_{l\sigma\mathbf{k}}^\dagger c_{l\sigma\mathbf{k}} + V_{x,l}^{\sigma\bar{\sigma}}(\mathbf{k}) c_{l\sigma\mathbf{k}}^\dagger c_{l\bar{\sigma}\mathbf{k}}] - \sum_{\mathbf{k}, \sigma, \sigma'} \Delta_{\mathbf{k}}^{\sigma\sigma'} c_{t\sigma\mathbf{k}}^\dagger c_{b\sigma'\mathbf{k}} - \text{H.c.} \quad (6)$$

We have explicitly separated \hat{V}_{HF} into Hartree potentials $V_{H,l}$, intralayer exchange potentials between the same spin $V_{x,l}^{\sigma\sigma}(\mathbf{k})$, intralayer exchange potentials between opposite spins $V_{x,l}^{\sigma\bar{\sigma}}(\mathbf{k})$, and interlayer exchange potentials $\Delta_{\mathbf{k}}^{\sigma\sigma'}$.

In the matrix form with spinor basis $(c_{t\uparrow\mathbf{k}} \ c_{t\downarrow\mathbf{k}} \ c_{b\uparrow\mathbf{k}} \ c_{b\downarrow\mathbf{k}})^T$, the HF Hamiltonian $\hat{H}_{\text{HF}}(\mathbf{k}) = \hat{H}_0(\mathbf{k}) + \hat{V}_{\text{HF}}(\mathbf{k})$ is given by

$$\hat{H}_{\text{HF}}(\mathbf{k}) = \begin{pmatrix} \varepsilon_0(\mathbf{k}) + V_{H,t} + V_{x,t}^{\uparrow\uparrow}(\mathbf{k}) & V_{x,t}^{\uparrow\downarrow}(\mathbf{k}) & -\Delta_{\mathbf{k}}^{\uparrow\uparrow} & -\Delta_{\mathbf{k}}^{\uparrow\downarrow} \\ V_{x,t}^{\downarrow\uparrow}(\mathbf{k}) & \varepsilon_0(\mathbf{k}) + V_{H,t} + V_{x,t}^{\downarrow\downarrow}(\mathbf{k}) & -\Delta_{\mathbf{k}}^{\downarrow\uparrow} & -\Delta_{\mathbf{k}}^{\downarrow\downarrow} \\ -\Delta_{\mathbf{k}}^{*\uparrow\uparrow} & -\Delta_{\mathbf{k}}^{*\uparrow\downarrow} & \varepsilon_0(\mathbf{k}) + V_{H,b} + V_{x,b}^{\uparrow\uparrow}(\mathbf{k}) & V_{x,b}^{\uparrow\downarrow}(\mathbf{k}) \\ -\Delta_{\mathbf{k}}^{*\downarrow\uparrow} & -\Delta_{\mathbf{k}}^{*\downarrow\downarrow} & V_{x,b}^{\downarrow\uparrow}(\mathbf{k}) & \varepsilon_0(\mathbf{k}) + V_{H,b} + V_{x,b}^{\downarrow\downarrow}(\mathbf{k}) \end{pmatrix}. \quad (7)$$

The electrostatic Hartree potentials are

$$V_{H,l} = \frac{2\pi e^2 d}{\epsilon} n_l, \quad (8)$$

where n_l is the carrier density in layer l ,

$$n_l = \frac{1}{A} \sum_{\mathbf{k}, \sigma} \rho_{ll}^{\sigma\sigma}(\mathbf{k}), \quad (9)$$

and $\rho(\mathbf{k})$ is the density matrix with matrix elements

$$\rho_{ll'}^{\sigma\sigma'}(\mathbf{k}) = \langle c_{l\sigma\mathbf{k}}^\dagger c_{l'\sigma'\mathbf{k}} \rangle. \quad (10)$$

The expectation is taken in the ground state. The intralayer exchange potentials are

$$V_{x,l}^{\sigma\sigma'}(\mathbf{k}) = -\frac{1}{A} \sum_{\mathbf{k}'} V_{\mathbf{k}-\mathbf{k}'}^S \rho_{ll}^{\sigma\sigma'}(\mathbf{k}'), \quad (11)$$

and the interlayer exchange terms are

$$\Delta_{\mathbf{k}}^{\sigma\sigma'} = \frac{1}{A} \sum_{\mathbf{k}'} V_{\mathbf{k}-\mathbf{k}'}^D \rho_{tb}^{\sigma\sigma'}(\mathbf{k}'). \quad (12)$$

The HF total energy is the sum of all contributions,

$$E_{\text{tot}} = \sum_{\mathbf{k}, l, \sigma} \left(\varepsilon_0(\mathbf{k}) + \frac{1}{2} V_{H,l} \right) \rho_{ll}^{\sigma\sigma}(\mathbf{k}) + \frac{1}{2} \sum_{\mathbf{k}, l, \sigma, \sigma'} V_{x,l}^{\sigma\sigma'}(\mathbf{k}) \rho_{ll}^{\sigma'\sigma}(\mathbf{k}) - \frac{1}{2} \sum_{\mathbf{k}, \sigma, \sigma'} [\Delta_{\mathbf{k}}^{\sigma\sigma'} \rho_{bt}^{\sigma'\sigma}(\mathbf{k}) + \text{c.c.}]. \quad (13)$$

The first (noninteracting single-particle) term includes the kinetic energy and electrostatic Hartree energy, the second and the last (interacting) terms are intralayer and interlayer exchange energies, respectively, arising from the Coulomb coupling.

In subsequent analyses, we use the effective Bohr radius a^* and the effective Rydberg Ry^* , defined as

$$a^* = \frac{\epsilon \hbar^2}{m^* e^2}, \quad \text{Ry}^* = \frac{e^2}{2a^* \epsilon} = \frac{\hbar^2}{2m^* (a^*)^2}, \quad (14)$$

as fundamental units of length and energy, respectively. In the semiconductor double quantum well structure GaAs-AlGaAs, $\epsilon = 12.5$, $m^* = 0.07m_e$ [66], $a^* = 98.3 \text{ \AA}$ and $\text{Ry}^* \approx 5.5 \text{ meV}$. In a 2DEG, the average distance between electrons is quantified by the dimensionless length scale r_s , which is related to the density n by

$$r_s a^* = \frac{1}{\sqrt{\pi n}}. \quad (15)$$

Our calculations are presented in terms of both dimensionless quantities (r_s, \tilde{d}), where $\tilde{d} = d/a^*$, and experimentally measurable parameters (n, d) using GaAs quantum well conduction band parameters. Some minor modifications are necessary for graphene, where the kinetic energy term is linearly dispersing, but our results remain qualitatively valid.

A. HF energy

Based on Eqs. (8)–(13), we explicitly show HF energies of the four competing ground states S_0, S_1, S_2 , and S_3 in

this subsection. An interlayer coherent state emerges from a superposition of electron states residing in the top and bottom layers. The eigenstates of this pseudospin polarization can be represented as a linear combination:

$$|\xi\rangle = \alpha|t\rangle + \beta|b\rangle, \quad |\bar{\xi}\rangle = \beta|t\rangle - \alpha|b\rangle, \quad (16)$$

where α and β can be taken as real numbers without loss of generality, and $\alpha^2 + \beta^2 = 1$ satisfying the normalization condition. The symmetric state $|\xi\rangle$ and antisymmetric state $|\bar{\xi}\rangle$ correspond to the lower and higher eigenenergies, respectively.

1. HF energy of the spin- and pseudospin-unpolarized state S_0

The wave function of the spin- and pseudospin-unpolarized state S_0 can be written as

$$\begin{aligned} |S_0\rangle &= \prod_{k \leq k_F} c_{\xi \uparrow \mathbf{k}}^\dagger c_{\xi \downarrow \mathbf{k}}^\dagger c_{\bar{\xi} \uparrow \mathbf{k}}^\dagger c_{\bar{\xi} \downarrow \mathbf{k}}^\dagger |0\rangle \\ &= \prod_{k \leq k_F} c_{t \uparrow \mathbf{k}}^\dagger c_{t \downarrow \mathbf{k}}^\dagger c_{b \uparrow \mathbf{k}}^\dagger c_{b \downarrow \mathbf{k}}^\dagger |0\rangle, \end{aligned} \quad (17)$$

where $|0\rangle$ is the vacuum state. There are four equal Fermi surfaces with Fermi momentum $k_F = \sqrt{\pi n}$. The densities and HF potentials of S_0 state are

$$\begin{aligned} n_t &= n_b = \frac{n}{2}, \\ \rho_{ll'}^{\sigma\sigma'}(\mathbf{k}) &= \delta_{ll'} \delta_{\sigma\sigma'} f_{\mathbf{k}}, \\ V_{H,t} &= V_{H,b} = \frac{\pi e^2 dn}{\epsilon}, \\ V_{x,l}^{\sigma\sigma'}(\mathbf{k}) &= -\frac{\delta_{\sigma\sigma'}}{A} \sum_{k' \leq k_F} \frac{2\pi e^2}{\epsilon |\mathbf{k} - \mathbf{k}'|}, \\ \Delta_{\mathbf{k}}^{\sigma\sigma'} &= 0, \end{aligned} \quad (18)$$

where $f_{\mathbf{k}}$ is the Fermi-Dirac distribution.

The kinetic energy E_{kin} , Hartree energy E_{H} , exchange energy of the intralayer interaction E_x^{intra} , and the interlayer interaction E_x^{inter} are, respectively,

$$\begin{aligned} E_{\text{kin}} &= 4 \sum_{k \leq k_F} \frac{\hbar^2 k^2}{2m^*} = \frac{\pi \hbar^2 A}{4m^*} n^2, \\ E_{\text{H}} &= 0, \\ E_x^{\text{intra}} &= -\frac{2}{A} \sum_{k, k' \leq k_F} \frac{2\pi e^2}{\epsilon |\mathbf{k} - \mathbf{k}'|} = -\frac{4e^2 A}{3\sqrt{\pi}\epsilon} n^{3/2}, \\ E_x^{\text{inter}} &= 0. \end{aligned} \quad (19)$$

We have used the analytical integrations over momenta \mathbf{k} and \mathbf{k}' summarized in Appendix A. The HF energy $E_{\text{tot}}^{S_0}$ is the sum of these contributions in Eq. (19). The HF energy per electron $\varepsilon_{\text{tot}}^{S_0} = E_{\text{tot}}^{S_0}/nA$, expressed in terms of n and r_s , is

$$\begin{aligned} \varepsilon_{\text{tot}}^{S_0}(n) &= \frac{\pi \hbar^2}{4m^*} n - \frac{4e^2}{3\sqrt{\pi}\epsilon} n^{1/2}, \\ \varepsilon_{\text{tot}}^{S_0}(r_s) &= \left[\frac{1}{r_s^2} - \frac{8\sqrt{2}}{3\pi r_s} \right] \text{Ry}^*. \end{aligned} \quad (20)$$

$r_s a^* = r_{s,t} a^* = r_{s,b} a^* = \sqrt{2/\pi n}$, here $r_{s,t}$ and $r_{s,b}$ are inter-electron distance in the top and bottom layers, respectively.

2. HF energy of the spin-polarized but pseudospin-unpolarized state S_1

The wave function of the spin-polarized but pseudospin-unpolarized state S_1 is

$$\begin{aligned} |S_1\rangle &= \prod_{k \leq k_F} c_{\xi \uparrow \mathbf{k}}^\dagger c_{\bar{\xi} \uparrow \mathbf{k}}^\dagger |0\rangle \\ &= \prod_{k \leq k_F} c_{b \uparrow \mathbf{k}}^\dagger c_{t \uparrow \mathbf{k}}^\dagger |0\rangle. \end{aligned} \quad (21)$$

There are two equal Fermi surfaces with Fermi momentum $k_F = \sqrt{2\pi n}$. The densities and HF potentials of S_1 state are

$$\begin{aligned} n_t &= n_b = \frac{n}{2}, \\ \rho_{ll'}^{\sigma\sigma'}(\mathbf{k}) &= \delta_{ll'} \delta_{\sigma\sigma'} \delta_{\uparrow\sigma} f_{\mathbf{k}}, \\ V_{H,t} &= V_{H,b} = \frac{\pi e^2 dn}{\epsilon}, \\ V_{x,l}^{\sigma\sigma'}(\mathbf{k}) &= -\frac{\delta_{\sigma\sigma'} \delta_{\uparrow\sigma}}{A} \sum_{k' \leq k_F} \frac{2\pi e^2}{\epsilon |\mathbf{k} - \mathbf{k}'|}, \\ \Delta_{\mathbf{k}}^{\sigma\sigma'} &= 0. \end{aligned} \quad (22)$$

We have assumed the majority spin to be $\sigma = \uparrow$. The energies are

$$\begin{aligned} E_{\text{kin}} &= 2 \sum_{k \leq k_F} \frac{\hbar^2 k^2}{2m^*} = \frac{\pi \hbar^2 A}{2m^*} n^2, \\ E_{\text{H}} &= 0, \\ E_x^{\text{intra}} &= -\frac{1}{A} \sum_{k, k' \leq k_F} \frac{2\pi e^2}{\epsilon |\mathbf{k} - \mathbf{k}'|} = -\frac{4\sqrt{2}e^2 A}{3\sqrt{\pi}\epsilon} n^{3/2}, \\ E_x^{\text{inter}} &= 0. \end{aligned} \quad (23)$$

The HF energy per electron

$$\begin{aligned} \varepsilon_{\text{tot}}^{S_1}(n) &= \frac{\pi \hbar^2}{2m^*} n - \frac{4\sqrt{2}e^2}{3\sqrt{\pi}\epsilon} n^{1/2}, \\ \varepsilon_{\text{tot}}^{S_1}(r_s) &= \left[\frac{2}{r_s^2} - \frac{16}{3\pi r_s} \right] \text{Ry}^*, \end{aligned} \quad (24)$$

and $r_s a^* = r_{s,t} a^* = r_{s,b} a^* = \sqrt{2/\pi n}$.

3. HF energy of the spin-polarized interlayer coherent state S_ξ

The wave function of the spin-polarized interlayer coherent (pseudospin-polarized) state S_ξ is

$$\begin{aligned} |S_\xi\rangle &= \prod_{k \leq k_F} c_{\xi \uparrow \mathbf{k}}^\dagger |0\rangle \\ &= \prod_{k \leq k_F} (\alpha c_{t \uparrow \mathbf{k}}^\dagger + \beta c_{b \uparrow \mathbf{k}}^\dagger) |0\rangle. \end{aligned} \quad (25)$$

The pseudospin is in a direction with polar angle $\theta = 2 \arctan(\alpha/\beta)$ with a freedom of any azimuthal angle ϕ even though we specifically choose α, β to be real. There is only

one Fermi surface with Fermi momentum $k_F = \sqrt{4\pi n}$ for the pseudospin fully polarized state. The densities and HF potentials of S_ξ state are

$$\begin{aligned} n_t &= n\alpha^2, \quad n_b = n\beta^2, \\ \rho_{ll'}^{\sigma\sigma'}(\mathbf{k}) &= \delta_{\sigma\sigma'}\delta_{\uparrow\sigma}[\delta_{ll'}\delta_{lt}\alpha^2 + \delta_{ll'}\delta_{lb}\beta^2 + (1 - \delta_{ll'})\alpha\beta]f_{\mathbf{k}}, \\ V_{H,l} &= \frac{2\pi e^2 dn}{\epsilon}[\delta_{ll'}\delta_{lt}\alpha^2 + \delta_{ll'}\delta_{lb}\beta^2], \\ V_{x,l}^{\sigma\sigma'}(\mathbf{k}) &= -[\delta_{ll'}\delta_{lt}\alpha^2 + \delta_{ll'}\delta_{lb}\beta^2]\frac{\delta_{\sigma\sigma'}\delta_{\uparrow\sigma}}{A}\sum_{k' \leq k_F}\frac{2\pi e^2}{\epsilon|\mathbf{k}' - \mathbf{k}|}, \\ \Delta_{\mathbf{k}}^{\sigma\sigma'} &= \alpha\beta\frac{\delta_{\sigma\sigma'}\delta_{\uparrow\sigma}}{A}\sum_{k' \leq k_F}\frac{2\pi e^2}{\epsilon|\mathbf{k}' - \mathbf{k}|}e^{-|\mathbf{k}' - \mathbf{k}|d}. \end{aligned} \quad (26)$$

The energies are

$$\begin{aligned} E_{\text{kin}} &= \sum_{k \leq k_F}\frac{\hbar^2 k^2}{2m^*} = \frac{\pi \hbar^2 A}{m^*}n^2, \\ E_H &= \frac{1}{2}\sum_{k \leq k_F}\frac{2\pi e^2 dn}{\epsilon}\frac{(\alpha^2 - \beta^2)^2}{2} \\ &= \frac{\pi e^2 d}{2\epsilon}n^2 A(\alpha^2 - \beta^2)^2, \\ E_x^{\text{intra}} &= -\frac{1}{2A}\sum_{k, k' \leq k_F}\frac{2\pi e^2}{\epsilon|\mathbf{k}' - \mathbf{k}|}(\alpha^4 + \beta^4) \\ &= -\frac{8e^2 A}{3\sqrt{\pi}\epsilon}n^{3/2}(\alpha^4 + \beta^4), \\ E_x^{\text{inter}} &= -\frac{1}{2A}\sum_{k, k' \leq k_F}\frac{2\pi e^2}{\epsilon|\mathbf{k} - \mathbf{k}'|}2\alpha^2\beta^2 e^{-|\mathbf{k} - \mathbf{k}'|d} \\ &= -\frac{2e^2 A\alpha^2\beta^2}{\sqrt{\pi}\epsilon}n^{3/2}J(k_F d), \end{aligned} \quad (27)$$

where $J(k_F d)$ is the triple integral

$$J(k_F d) = \int_0^1 dx x \int_0^1 dy y \int_0^{2\pi} d\theta \frac{e^{-k_F d \sqrt{x^2 + y^2 - 2xy \cos \theta}}}{\sqrt{x^2 + y^2 - 2xy \cos \theta}}, \quad (28)$$

which should be evaluated numerically. The HF energy per electron is

$$\begin{aligned} \varepsilon_{\text{tot}}^{S_\xi}(n) &= \frac{\pi \hbar^2}{m^*}n + \frac{\pi e^2 d}{2\epsilon}n(\alpha^2 - \beta^2)^2 \\ &\quad - \frac{8e^2}{3\sqrt{\pi}\epsilon}n^{1/2}\left(\alpha^4 + \beta^4 + \frac{3}{4}J(k_F d)\alpha^2\beta^2\right). \end{aligned} \quad (29)$$

Represented in dimensionless length using $r_{s,l}a^* = 1/\sqrt{\pi n_l}$ and

$$\begin{aligned} \pi(n_t + n_b) &= \pi n \\ &= \left(\frac{1}{r_{s,t}^2} + \frac{1}{r_{s,b}^2}\right)\frac{1}{(a^*)^2} \\ &\equiv \frac{1}{(\tilde{r}_s a^*)^2}, \end{aligned} \quad (30)$$

the HF energy per electron is

$$\begin{aligned} \varepsilon_{\text{tot}}^{S_\xi}(\tilde{r}_s) &= \left[\frac{2}{\tilde{r}_s^2} + \frac{d}{a^* \tilde{r}_s^2}(\alpha^2 - \beta^2)^2 \right. \\ &\quad \left. - \frac{16}{3\pi \tilde{r}_s}\left(\alpha^4 + \beta^4 + \frac{3}{4}J(k_F d)\alpha^2\beta^2\right)\right] \text{Ry}^*. \end{aligned} \quad (31)$$

Note that $\tilde{r}_s \equiv \tilde{r}_s(r_{s,t}, r_{s,b})$.

In particular, the S_3 phase, the spin-polarized interlayer coherent state with pseudospin polarized in the z direction (polar angle $\theta = 0$), is the case that all electrons are in one layer but not the other, i.e., $\alpha = 1$, $\beta = 0$, $\tilde{r}_s = r_{s,t}$, and $r_{s,b} \rightarrow \infty$. The HF energy of S_3 phase is

$$\begin{aligned} \varepsilon_{\text{tot}}^{S_3}(n) &= \frac{\pi \hbar^2}{m^*}n + \frac{\pi e^2}{2\epsilon}nd - \frac{8e^2}{3\sqrt{\pi}\epsilon}n^{1/2}, \\ \varepsilon_{\text{tot}}^{S_3}(\tilde{r}_s) &= \left[\frac{2}{\tilde{r}_s^2} + \frac{d}{a^* \tilde{r}_s^2} - \frac{16}{3\pi \tilde{r}_s}\right] \text{Ry}^*. \end{aligned} \quad (32)$$

The S_2 phase, the spin-polarized interlayer coherent state with pseudospin polarized in the xy plane (polar angle $\theta = \pi/2$), is the case of equal layer densities, i.e., $\alpha^2 = \beta^2 = \frac{1}{2}$, $r_s = r_{s,t} = r_{s,b} = \sqrt{2}\tilde{r}_s$. The HF energy per electron of S_2 phase is

$$\begin{aligned} \varepsilon_{\text{tot}}^{S_2}(n) &= \frac{\pi \hbar^2}{m^*}n - \frac{4e^2}{3\sqrt{\pi}\epsilon}n^{1/2}\left(1 + \frac{3}{8}J(k_F d)\right), \\ \varepsilon_{\text{tot}}^{S_2}(r_s) &= \left[\frac{4}{r_s^2} - \frac{8\sqrt{2}}{3\pi r_s}\left(1 + \frac{3}{8}J(k_F d)\right)\right] \text{Ry}^*, \\ \varepsilon_{\text{tot}}^{S_2}(\tilde{r}_s) &= \left[\frac{2}{\tilde{r}_s^2} - \frac{8}{3\pi \tilde{r}_s}\left(1 + \frac{3}{8}J(k_F d)\right)\right] \text{Ry}^*. \end{aligned} \quad (33)$$

The triple integral $J(k_F d)$ defined in Eq. (28) has the properties that

$$\begin{aligned} 0 &\leq J(k_F d) \leq \frac{8}{3}, \\ J(0) &= \frac{8}{3}, \\ \lim_{k_F d \gg 1} J(k_F d) &\rightarrow 0. \end{aligned} \quad (34)$$

As expected, for $d = 0$,

$$\begin{aligned} \lim_{d \rightarrow 0} \varepsilon_{\text{tot}}^{S_2}(n) &\rightarrow \frac{\pi \hbar^2}{m^*}n - \frac{8e^2}{3\sqrt{\pi}\epsilon}n^{1/2}, \\ \lim_{d \rightarrow 0} \varepsilon_{\text{tot}}^{S_2}(r_s) &\rightarrow \left[\frac{4}{r_s^2} - \frac{16\sqrt{2}}{3\pi r_s}\right] \text{Ry}^*, \end{aligned} \quad (35)$$

which recovers the energy of single 2DEG with one Fermi surface.

For $0 < k_F d \ll 1$, $J(k_F d)$ can be expanded in Taylor series

$$\begin{aligned} J(k_F d) &= J(0) - \frac{\pi}{2}k_F d + \frac{1}{2}(k_F d)^2 \int_0^1 dx x \int_0^1 dy y \int_0^{2\pi} d\theta \\ &\quad \times \sqrt{x^2 + y^2 - 2xy \cos \theta} + \dots \end{aligned} \quad (36)$$

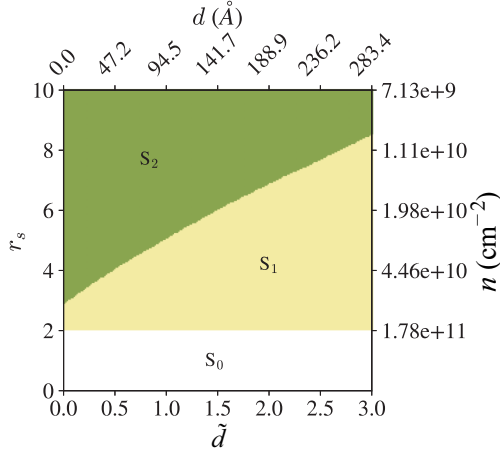


FIG. 2. The zero-temperature phase diagram with respect to r_s and \tilde{d} , where $\tilde{d} = d/a^*$. Dimensionless r_s and \tilde{d} are also converted to density n in the unit of cm^{-2} and distance d in the unit of \AA using GaAs quantum well parameters. S_0 , S_1 , and S_2 phases all have equal layer densities, i.e., $r_s a^* = r_{st} a^* = r_{sb} a^* = \sqrt{2/\pi n}$.

B. Phase diagram for equal layer densities

The S_2 phase with XY easy-plane pseudospin ordering always has a lower energy than the Ising-ordered S_3 phase (with all electrons in one layer with pseudospin polarized along z direction) because the density imbalance between the layers in S_3 pays an extra Hartree energy. This preference is also inferred from Eqs. (32) and (33) by taking their energy difference:

$$\begin{aligned} \varepsilon_{\text{tot}}^{S_2}(n) - \varepsilon_{\text{tot}}^{S_3}(n) &= -\frac{4e^2}{3\sqrt{\pi\epsilon}} n^{1/2} \left(\frac{3}{8} J(k_F d) - 1 \right) - \frac{\pi e^2}{2\epsilon} n d \\ &= -\frac{e^2 k_F}{4\pi\epsilon} \left[J(k_F d) - \frac{8}{3} + \frac{\pi}{2} k_F d \right]. \end{aligned} \quad (37)$$

The function $J(z)$ monotonically decreases with z and intersects with the line $-\pi z/2 + \frac{8}{3}$ at $z = 0$, the slope of which equals the derivative of $J(z)$ at $z = 0$,

$$\left. \frac{dJ(z)}{dz} \right|_{z=0} = -\frac{\pi}{2}. \quad (38)$$

It follows that

$$\varepsilon_{\text{tot}}^{S_2} - \varepsilon_{\text{tot}}^{S_3} < 0 \quad \forall k_F d > 0. \quad (39)$$

This energetic hierarchy is shown by the computed HF energies as a function of layer separation d in Appendix B.

The zero-temperature phase diagram, determined by $\varepsilon_{\text{tot}}^G = \min\{\varepsilon_{\text{tot}}^{S_0}, \varepsilon_{\text{tot}}^{S_1}, \varepsilon_{\text{tot}}^{S_2}\}$, with respect to r_s and \tilde{d} is shown in Fig. 2. The interlayer coherent phase S_2 manifests stability at larger r_s (lower electron density) and smaller interlayer distance \tilde{d} . Note that there is always a critical r_s for the transition to the interlayer coherent phase, which is stable only above a specific d -dependent r_s value, with the critical r_s increasing with increasing d .

C. Phase diagram for unequal layer densities

When the two layers have unequal densities, the spin polarization of each layer individually depends on the layer density: if the layer density is larger (smaller) than the critical value corresponding to $r_s \sim 2$, the spin-unpolarized (spin-polarized) phase is favored. The phase that the lower-density layer is spin polarized and the higher-density layer is spin unpolarized has been identified in a previous theoretical study [67] as the three-component phase. In the rest of the paper, we assume the density in each layer is lower than this critical value of the ferromagnetic instability ($r_s \sim 2$) and therefore will only consider the spin-polarized case because spin plays no role in the interlayer coherence physics. For unequal layer densities, we compare HF energies of the interlayer coherent phase S_ξ in Eq. (29) with the interlayer incoherent phase S'_1 . The S'_1 phase is the generalized case of S_1 phase (defined in Sec. III A 2) but with two unequal Fermi surfaces. It is straightforward to write the HF energy per electron of S'_1 phase, represented in total density n and layer polarization $m = (n_t - n_b)/n$:

$$\begin{aligned} \varepsilon_{\text{tot}}^{S'_1}(n, m) &= \frac{\pi \hbar^2}{2m^*} n(1 + m^2) + \frac{\pi e^2 d}{2\epsilon} n m^2 \\ &\quad - \frac{2\sqrt{2}e^2}{3\sqrt{\pi\epsilon}} n^{1/2} [(1 + m)^{3/2} + (1 - m)^{3/2}]. \end{aligned} \quad (40)$$

For a direct comparison, we represent the HF energy of S_ξ phase in Eq. (29) using n and m as well:

$$\begin{aligned} \varepsilon_{\text{tot}}^{S_\xi}(n, m) &= \frac{\pi \hbar^2}{m^*} n + \frac{\pi e^2 d}{2\epsilon} n m^2 \\ &\quad - \frac{4e^2}{3\sqrt{\pi\epsilon}} n^{1/2} \left[1 + m^2 + \frac{3}{8} J(k_F d)(1 - m^2) \right]. \end{aligned} \quad (41)$$

For layer-unpolarized case $m = 0$, S'_1 phase is equivalent to the pseudospin-unpolarized phase S_1 , $\varepsilon_{\text{tot}}^{S'_1}(n, m = 0) = \varepsilon_{\text{tot}}^{S_1}(n)$. For the totally layer-polarized case $m = 1$, S'_1 phase is equivalent to S_ξ , there is only one Fermi surface and no interlayer coherence because one layer is completely empty.

In Figs. 3(a)–3(d) we plot the energy difference $\varepsilon_{\text{tot}}^{S'_1} - \varepsilon_{\text{tot}}^{S_\xi}$ as a function of layer polarization m and interlayer separation \tilde{d} for several fixed total densities. The corresponding \tilde{r}_s (defined by the total density $\tilde{r}_s a^* = \sqrt{1/\pi n}$) and \bar{r}_s (defined by the average layer density $\bar{r}_s a^* = \sqrt{2/\pi n}$) are labeled in each subplot. Similarly, Figs. 3(e)–3(h) plot $\varepsilon_{\text{tot}}^{S'_1} - \varepsilon_{\text{tot}}^{S_\xi}$ as a function of \tilde{r}_s and m for several fixed-layer separations. As m increases, the phase boundary shifts to larger \tilde{d} [Figs. 3(a)–3(d)] and smaller \tilde{r}_s [Figs. 3(e)–3(h)], indicating that the interlayer coherent phase S_ξ is more preferred than the interlayer incoherent phase S'_1 for larger m . We conclude from Fig. 3 that the interlayer coherent phase S_ξ is preferred for all $m \in [0, 1)$.

For the two interlayer incoherent phases S_1 and S'_1 , their energy difference depends on layer polarization m by

$$\begin{aligned} \varepsilon_{\text{tot}}^{S'_1} - \varepsilon_{\text{tot}}^{S_1} &= \frac{\pi \hbar^2}{2m^*} n m^2 + \frac{\pi e^2 d}{2\epsilon} n m^2 - \frac{2\sqrt{2}e^2}{3\sqrt{\pi\epsilon}} \\ &\quad \times n^{1/2} [(1 + m)^{3/2} + (1 - m)^{3/2} - 2]. \end{aligned} \quad (42)$$

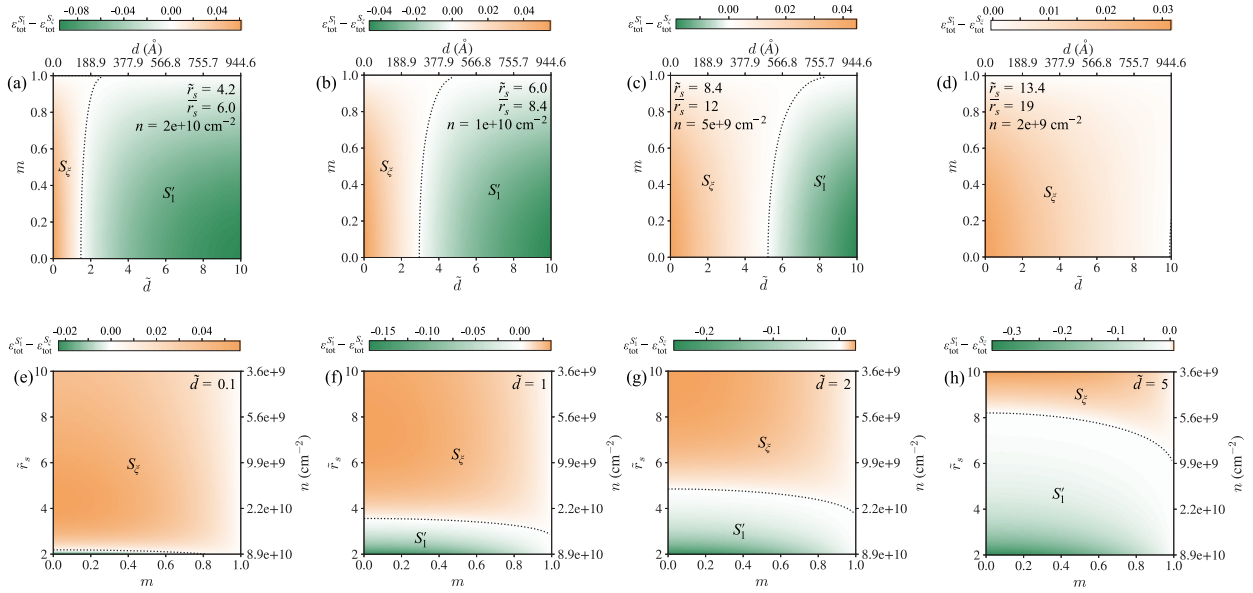


FIG. 3. Energy difference $\varepsilon_{\text{tot}}^{S'_1} - \varepsilon_{\text{tot}}^{S'_\xi}$. (a)–(d) As a function of layer polarization m and \bar{d} for fixed total densities $n = 2 \times 10^{10} \text{ cm}^{-2}$, 10^{10} cm^{-2} , $5 \times 10^9 \text{ cm}^{-2}$, and $2 \times 10^9 \text{ cm}^{-2}$. The corresponding \bar{r}_s (defined by the total density $\bar{r}_s a^* = \sqrt{1/\pi n}$) and \tilde{r}_s (defined by the averaged layer density $\tilde{r}_s a^* = \sqrt{2/\pi n}$) are labeled in each subplot. (e)–(h) As a function of \tilde{r}_s and m for fixed $\bar{d} = 0.1, 1, 2,$ and 5 . The dotted lines trace the phase boundaries. As m increases, the phase boundary tilts to larger \bar{d} and smaller \tilde{r}_s , indicating that the interlayer coherent phase S'_ξ is more preferred for larger m .

Expand in m ,

$$\frac{\varepsilon_{\text{tot}}^{S'_1} - \varepsilon_{\text{tot}}^{S'_\xi}}{\text{Ry}^*} = \pi a^* m^2 \sqrt{n} \left[(a^* + d) \sqrt{n} - \frac{\sqrt{2}}{\pi^{3/2}} \right] + O(m^4), \quad (43)$$

where $\varepsilon_{\text{tot}}^{S'_1} - \varepsilon_{\text{tot}}^{S'_\xi} < 0$ only for small n and small d .

In Fig. 4, we show phase diagrams as a function of m and \bar{d} for fixed total densities, chosen to be the same as in Figs. 3(a)–3(d). The phase diagrams are determined by the lowest energy $\min\{\varepsilon_{\text{tot}}^{S'_1}, \varepsilon_{\text{tot}}^{S'_\xi}, \varepsilon_{\text{tot}}^{S'_\xi}\}$. In these phase diagrams, the S'_1 phase is never the ground state, even for larger \bar{d} where S'_1 is lower in energy than S'_ξ as in Figs. 3(a)–3(d). This is because the critical \bar{d} for $\varepsilon_{\text{tot}}^{S'_1} - \varepsilon_{\text{tot}}^{S'_\xi} < 0$ is smaller than that of the phase boundary in Figs. 3(a)–3(d).

For $m \rightarrow 1$, the phase boundary in Fig. 4 can be understood analytically by examining the energy difference between the interlayer coherent phase S'_ξ and incoherent phase S'_1 :

$$\begin{aligned} \frac{\varepsilon_{\text{tot}}^{S'_\xi} - \varepsilon_{\text{tot}}^{S'_1}}{\text{Ry}^*} &= \pi n a^* [a^* + d(\alpha^2 - \beta^2)^2] \\ &+ \frac{n^{1/2} a^*}{\pi^{1/2}} \left[4\alpha^2 \beta^2 \left(\frac{8}{3} - J(k_F d) \right) - \frac{8(2 - \sqrt{2})}{3} \right] \\ &= \pi n a^* [a^* + d m^2] + \frac{n^{1/2} a^*}{\pi^{1/2}} \\ &\times \left[(1 - m^2) \left(\frac{8}{3} - J(k_F d) \right) - \frac{8(2 - \sqrt{2})}{3} \right]. \end{aligned} \quad (44)$$

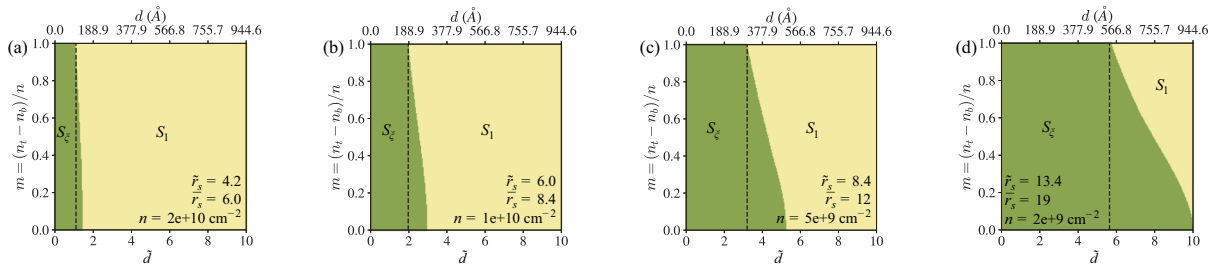


FIG. 4. Phase diagrams as a function of layer polarization m and \bar{d} for fixed total densities $n = 2 \times 10^{10} \text{ cm}^{-2}$, 10^{10} cm^{-2} , $5 \times 10^9 \text{ cm}^{-2}$, and $2 \times 10^9 \text{ cm}^{-2}$. The phase diagrams are determined by finding the lowest energy $\min\{\varepsilon_{\text{tot}}^{S'_1}, \varepsilon_{\text{tot}}^{S'_\xi}, \varepsilon_{\text{tot}}^{S'_\xi}\}$. The corresponding \bar{r}_s (defined by the total density $\bar{r}_s a^* = \sqrt{1/\pi n}$) and \tilde{r}_s (defined by the averaged layer density $\tilde{r}_s a^* = \sqrt{2/\pi n}$) are labeled in each subplot. The black dashed lines plot the critical distance \bar{d}_c in Eq. (53), converging precisely to the phase transition boundary for $m \rightarrow 1$ and for $n \rightarrow n_{\text{max}}$ as estimated in Eq. (52).

When $m \rightarrow 1$,

$$\lim_{m \rightarrow 1} \frac{\varepsilon_{\text{tot}}^{S_\xi} - \varepsilon_{\text{tot}}^{S_1}}{\text{Ry}^*} = \pi n a^* (a^* + d) - \frac{n^{1/2} a^* 8(2 - \sqrt{2})}{\pi^{1/2} 3}, \quad (45)$$

setting it to zero, we find that

$$\tilde{d}_c|_{m=1} \equiv \frac{d_c}{a^*} \Big|_{m=1} = \frac{8(2 - \sqrt{2})}{3} \frac{1}{\pi^{3/2} n^{1/2} a^*} - 1, \quad (46)$$

which only depends on total density n . The \tilde{d}_c in Eq. (46) is shown in black dashed lines in Fig. 4, they agree well with the phase boundary when $m \rightarrow 1$.

In fact, if we take a close look at the second line of Eq. (44), setting it to zero gives

$$\pi^{3/2} n^{1/2} (a^* + d_c m^2) + \left[(1 - m^2) \left(\frac{8}{3} - J(k_F d_c) \right) - \frac{8(2 - \sqrt{2})}{3} \right] = 0. \quad (47)$$

The first term $\pi^{3/2} n^{1/2} (a^* + d_c m^2)$ is positive; the only way that a d_c exists is that the second term is negative, which requires

$$J(k_F d_c) > \frac{8}{3} - \frac{8(2 - \sqrt{2})}{3(1 - m^2)}. \quad (48)$$

Given that $J(k_F d_c) \in [0, \frac{8}{3}]$ and it decays rapidly with $k_F d_c$, i.e., with $n^{1/2} d_c$, the competition between the first and the second terms in Eq. (47) in solving for a d_c , if it exists, ultimately requires $k_F d_c$ to be small for large n , and validates the approximation

$$J(k_F d) \approx \frac{8}{3} - \frac{\pi}{2} k_F d, \quad (49)$$

which are the first two terms in the expansion of Eq. (36). Substituting Eq. (49) to (47), we have

$$\tilde{d}_c|_{n \rightarrow n_{\text{max}}} = \frac{8(2 - \sqrt{2})}{3} \frac{1}{\pi^{3/2} n^{1/2} a^*} - 1. \quad (50)$$

The m dependence of d_c vanishes for large densities, and this critical distance d_c equals the one for $m \rightarrow 1$ case in Eq. (46). Taking $m \rightarrow 0$, Eq. (47) becomes

$$J(k_F d_c) = \pi^{3/2} n^{1/2} a^* + \frac{8(\sqrt{2} - 1)}{3}. \quad (51)$$

Because $J(k_F d_c) \leq \frac{8}{3}$, we could find that the maximum density for a d_c to exist is

$$n_{\text{max}} \sim 8.8 \times 10^{10} \text{ cm}^{-2}. \quad (52)$$

From the discussion above, we find that the critical distance \tilde{d}_c at these two limits, $m \rightarrow 1$ and $n \rightarrow n_{\text{max}}$, turns out to be the same value

$$\begin{aligned} \tilde{d}_c|_{m=1} &= \tilde{d}_c|_{n \rightarrow n_{\text{max}}} \\ &= \frac{8(2 - \sqrt{2})}{3} \frac{1}{\pi^{3/2} n^{1/2} a^*} - 1. \end{aligned} \quad (53)$$

This explains the agreement between the phase boundary and the black dashed lines in Fig. 4, when either the layer density imbalance is large, as in Figs. 4(a)–4(d) at $m \rightarrow 1$, or the total density is close to n_{max} , as in Fig. 4(a).

In Fig. 4, the phase transition boundary \tilde{d}_c decreases with layer polarization m , revealing that a layer density imbalance suppresses the interlayer coherent phase S_ξ . This suppression becomes weaker as total density n increases. When n approaches n_{max} , \tilde{d}_c becomes almost independent of m . As long as n remains below n_{max} , a \tilde{d}_c exists and the interlayer coherent phase survives even when the layer is almost completely polarized.

The HF energy of the interlayer coherent phase S_ξ monotonically increases with layer polarization m . As seen by taking the derivative of Eq. (41) with respect to m ,

$$\frac{d\varepsilon_{\text{tot}}^{S_\xi}}{dm} = \frac{e^2 n^{1/2} m}{\epsilon \sqrt{\pi}} \left(\pi^{3/2} n^{1/2} d + J(k_F d) - \frac{8}{3} \right), \quad (54)$$

the term in the brackets is always positive for $d > 0$, which is clear from the Taylor expansion in Eq. (36). Therefore,

$$\frac{d\varepsilon_{\text{tot}}^{S_\xi}}{dm} \geq 0, \quad \forall n \quad (55)$$

$\varepsilon_{\text{tot}}^{S_\xi}$ monotonically increases with layer polarization m for any density n . Among interlayer coherent phases S_ξ , the layer fully polarized phase S_3 always has the highest energy and the layer equally occupied phase S_2 has the lowest energy. If carriers in the two layers are allowed to transfer, the system is always stabilized to the pseudospin XY-ordered phase S_2 .

The layer polarization m can be interpreted as the pseudospin response to an effective pseudospin magnetic field applied in the z direction, which can be experimentally tuned by gate voltages. The bilayer system is trivially pseudospin polarized in the z direction by virtue of this effective magnetic field, which is zero for $m = 0$ and fully polarized in z direction for $m = 1$. Figure 4 illustrates that even when there is a strong effective pseudospin magnetic field polarizing the pseudospin completely in the z direction, the exchange-driven XY pseudospin ferromagnetic transition is little affected.

In Fig. 5, we fix $r_{s,b}$ and evaluate the phase diagram as a function of $(r_{s,t}, \tilde{d})$. Note that for $r_{s,t} \lesssim 2$ in Fig. 5, the top layer is spin unpolarized and the bottom layer is spin polarized (because $r_{s,b} > 2$ in all presented figures) in the ground state [67]. In $m \rightarrow 1$ limit, $n_t \rightarrow n$, $n_b \rightarrow 0$, and $r_{s,t} \ll r_{s,b}$,

$$\tilde{d}_c|_{m=1} = \frac{8(2 - \sqrt{2})}{3} \frac{r_{s,t}}{\pi} - 1 \quad (56)$$

which is linear in $r_{s,t}$. In $m \rightarrow -1$ limit, $n_t \rightarrow 0$, $n_b \rightarrow n$, and $r_{s,b} \ll r_{s,t}$,

$$\tilde{d}_c|_{m=-1} = \frac{8(2 - \sqrt{2})}{3} \frac{r_{s,b}}{\pi} - 1 \quad (57)$$

which is independent of $r_{s,t}$. In Fig. 5, we plot \tilde{d}_c in Eq. (46) in black dashed lines and it agrees well with the phase boundary when the density imbalance is large: linear in $r_{s,t}$ for $r_{s,t} \ll r_{s,b}$ and independent of $r_{s,t}$ for $r_{s,b} \ll r_{s,t}$.

To provide a comprehensive picture of the phase diagram, we present 3D plots of the critical distance \tilde{d}_c with respect to $(r_{s,t}, r_{s,b})$ in Figs. 6(a)–6(c) and with respect to (\bar{r}_s, m) in Figs. 6(d)–6(f). Particularly, we mark the line cuts of the phase boundary, i.e., \tilde{d}_c versus $r_{s,t}$ at $r_{s,b} = 10, 15$, and 30 in Figs. 6(a)–6(c), which can be directly compared with the phase transition boundary in Figs. 5(e)–6(g). Similarly, we

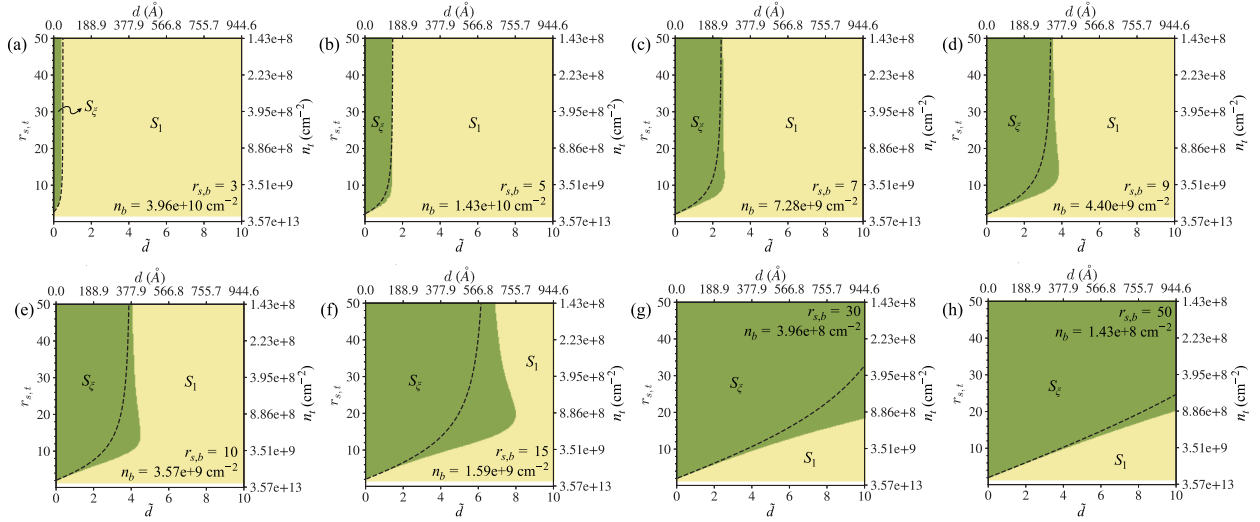


FIG. 5. Phase diagrams with respect to $(r_{s,t}, \tilde{d})$ for fixed $r_{s,b} \in [3, 50]$, corresponding to $n_b \sim \in [4 \times 10^{10}, 1.4 \times 10^8] \text{ cm}^{-2}$ in GaAs quantum wells. The black dashed lines plot the critical separation \tilde{d}_c in Eq. (53), which agrees well with the phase boundary when either the layer density imbalance is large or the total density is large: \tilde{d}_c is linear in $r_{s,t}$ for $r_{s,t} \ll r_{s,b}$ and independent of $r_{s,t}$ for $r_{s,b} \ll r_{s,t}$. Note that for $r_{s,t} \lesssim 2$, the top layer is spin unpolarized and the bottom layer is spin polarized (because $r_{s,b} > 2$ in all presented figures) in the ground state [67].

show the line cuts of the phase boundary \tilde{d}_c versus m at $\bar{r}_s = 8.4, 11.9,$ and 26.7 in Figs. 6(d)–6(f), as a direct comparison with the phase transition boundary in Figs. 4(b)–6(d).

To clearly trace the evolution of \tilde{d}_c with respect to tuning parameters m and \bar{r}_s , we show in Fig. 7(a) \tilde{d}_c versus m for six values of $\bar{r}_s \in [3.8, 30]$, in Fig. 7(b) \tilde{d}_c versus \bar{r}_s for six values of $m \in [0, 1]$. Figure 8 complements the trend of \tilde{d}_c with four additional plots that echo the configuration of Fig. 7(a), but with a refined set of $\bar{r}_s \in [4, 30]$. In scenarios of high electron density, corresponding to low \bar{r}_s as depicted in Fig. 8(a), we observe that \tilde{d}_c exhibits a negligible dependence on m . This aligns with our previous analysis in Eq. (53). The inset of

Fig. 8(a) illustrates this trend that as $n \rightarrow n_{\text{max}}$, \tilde{d}_c is independent of m and approaches zero.

D. Partially polarized pseudospin state

Previous subsections have been dedicated to examining interlayer coherent phases when the pseudospin is fully polarized, in the direction with polar angle $\theta = 2 \arctan(\alpha/\beta)$. However, the assumption of complete pseudospin polarization may not always hold, distinct from the sharp paramagnetic to ferromagnetic phase transition in the Bloch transition. This

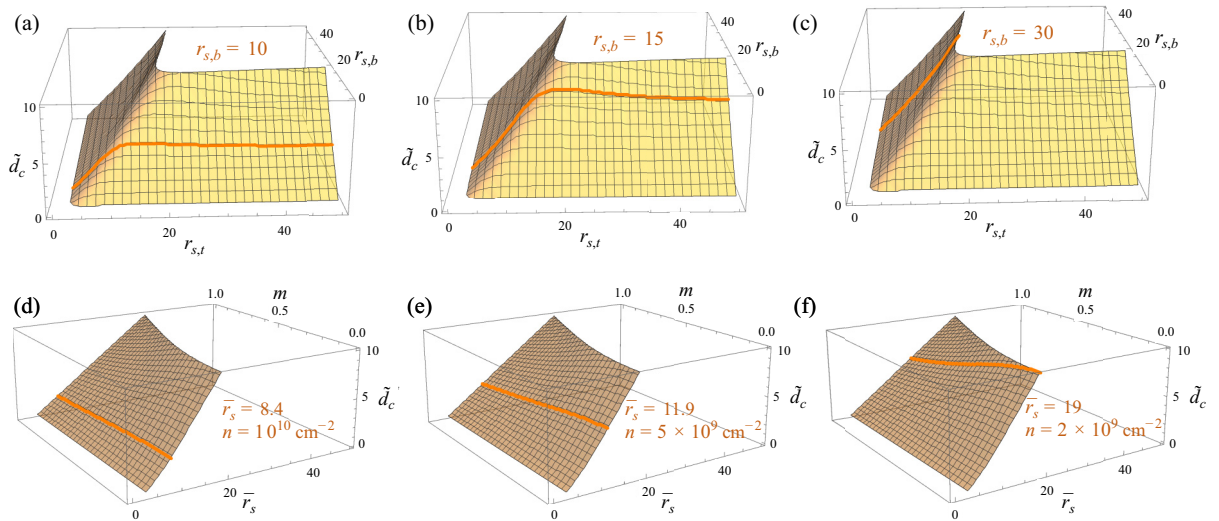


FIG. 6. 3D plots of the critical layer separation \tilde{d}_c . (a)–(c) With respect to $(r_{s,t}, r_{s,b})$. The orange line cuts trace the phase boundary \tilde{d}_c versus $r_{s,t}$ at $r_{s,b} = 10, 15,$ and 30 . These line cuts can be directly compared with the phase boundary in Figs. 5(e)–5(g). (d)–(f) With respect to (\bar{r}_s, m) , where \bar{r}_s is defined by the average layer density using $\bar{r}_s a^* = \sqrt{2/\pi n}$. The orange line cuts trace the phase boundary \tilde{d}_c versus m at $\bar{r}_s = 8.4, 11.9,$ and 26.7 . These line cuts can be directly compared with the phase boundary in Figs. 4(b)–4(d).

subsection extends our investigation to the HF energies associated with states of partial pseudospin polarization.

$$\hat{H}_{\text{HF}}^{S_2}(\mathbf{k}) = \begin{pmatrix} \varepsilon_0(\mathbf{k}) + V_{H,t} + V_{x,t}^{\uparrow\uparrow}(\mathbf{k}) & -\Delta_{\mathbf{k}}^{\uparrow\uparrow} & 0 & 0 \\ -(\Delta_{\mathbf{k}}^{\uparrow\uparrow})^* & \varepsilon_0(\mathbf{k}) + V_{H,b} + V_{x,b}^{\uparrow\uparrow}(\mathbf{k}) & 0 & 0 \\ 0 & 0 & \varepsilon_0(\mathbf{k}) + V_{H,t} & 0 \\ 0 & 0 & 0 & \varepsilon_0(\mathbf{k}) + V_{H,b} \end{pmatrix}, \quad (58)$$

and its four eigenvalues are

$$\begin{aligned} \varepsilon_{\mathbf{k}}^1 &= \varepsilon_0(\mathbf{k}) + V_{H,t}, \\ \varepsilon_{\mathbf{k}}^2 &= \varepsilon_0(\mathbf{k}) + V_{H,b}, \\ \varepsilon_{\mathbf{k}}^{\pm} &= \frac{1}{2}(\varepsilon_{t\mathbf{k}} + \varepsilon_{b\mathbf{k}}) \pm \sqrt{\xi_{\mathbf{k}}^2 + |\Delta_{\mathbf{k}}|^2}, \end{aligned} \quad (59)$$

where

$$\begin{aligned} \varepsilon_{t\mathbf{k}} &= \varepsilon_0(\mathbf{k}) + V_{H,t} + V_{x,t}^{\uparrow\uparrow}(\mathbf{k}), \\ \varepsilon_{b\mathbf{k}} &= \varepsilon_0(\mathbf{k}) + V_{H,b} + V_{x,b}^{\uparrow\uparrow}(\mathbf{k}), \\ \xi_{\mathbf{k}} &= \frac{1}{2}(\varepsilon_{t\mathbf{k}} - \varepsilon_{b\mathbf{k}}), \end{aligned} \quad (60)$$

and the HF potentials are in Eq. (26). The quasiparticle energy spectra are illustrated for two representative parameter sets: $r_s = 8$, $\tilde{d} = 1$ in Fig. 9(a) and $r_s = 4$, $\tilde{d} = 2.8$ in Fig. 9(b), corresponding to the two points marked by stars in the overall phase diagram in Fig. 9(c). In Figs. 9(a) and 9(b), the Fermi momentum is denoted by the vertical dotted line and the corresponding Fermi energy is denoted by the horizontal one. Notably, in Fig. 9(b), both quasiparticle bands ε^{\pm} are populated, which signals a deviation from the pseudospin fully polarized state, and we denote this phase as S_2' .

To crudely estimate the stability of this pseudospin partially polarized state, we compare the energy at zero momentum for the upper band ε_0^+ , with the energy at the Fermi momentum for the lower band $\varepsilon_{k_F}^-$, and show their difference across the (r_s, \tilde{d}) parameter space in Fig. 9(c). The red area corresponds to $\varepsilon_0^+ > \varepsilon_{k_F}^-$, i.e., stable S_2 phase [as in Fig. 9(a)],

The HF Hamiltonian of the spin-polarized (majority spin $\sigma = \uparrow$) interlayer coherent state is

and the blue area corresponds to $\varepsilon_0^+ < \varepsilon_{k_F}^-$, which we refer to as S_2' phase [the interlayer coherent phase characterized by two populated Fermi surfaces, as in Fig. 9(b)]. Compared to the previously obtained phase diagram in Fig. 2, the S_2' phase in Fig. 9(c) suggests that the interlayer coherent phase may persist over a broader range in the phase diagram than initially postulated when only fully polarized states were considered. But, the most accurate phase diagram should be determined by self-consistent HF calculations which will be discussed in Sec. IV. To quantify the stability of this partially polarized state, we extend our exploration of the HF energy to the S_2' phase, in which both quasiparticle states $|-, \mathbf{k}\rangle$ and $|+, \mathbf{k}\rangle$ are occupied. The generalization of the HF energy of the S_2 phase in Eqs. (27), (29), and (31) to the two-Fermi-surface case is systematic and monotonic, as detailed below.

The kinetic, Hartree, and exchange energies of the S_2' state, expressed in both Fermi momenta and densities, are

$$\begin{aligned} E_{\text{kin}} &= \frac{\hbar^2}{2m^*} \frac{A}{8\pi} (k_{F_-}^4 + k_{F_+}^4) \\ &= \frac{\hbar^2}{2m^*} \frac{A}{8\pi} 16\pi^2 (n_-^2 + n_+^2), \\ E_{\text{H}} &= \frac{e^2 d A}{32\epsilon\pi} (\alpha^2 - \beta^2)^2 (k_{F_-}^2 - k_{F_+}^2)^2 \\ &= \frac{e^2 d A}{32\epsilon\pi} (\alpha^2 - \beta^2)^2 16\pi^2 (n_- - n_+)^2, \\ E_x^{\text{intra}} &= -\frac{e^2 A}{\epsilon\pi^2} \left[\frac{1}{3} (\alpha^4 + \beta^4) (k_{F_-}^3 + k_{F_+}^3) \right. \\ &\quad \left. + \frac{1}{4} \alpha^2 \beta^2 \left[k_{F_+}^3 J\left(0, \frac{k_{F_-}}{k_{F_+}}\right) + k_{F_-}^3 J\left(0, \frac{k_{F_+}}{k_{F_-}}\right) \right] \right], \\ E_x^{\text{inter}} &= -\frac{e^2 A \alpha^2 \beta^2}{4\pi^2 \epsilon} \left\{ k_{F_-}^3 \left[J(k_{F_-} d, 1) - J\left(k_{F_-} d, \frac{k_{F_+}}{k_{F_-}}\right) \right] \right. \\ &\quad \left. + k_{F_+}^3 \left[J(k_{F_+} d, 1) - J\left(k_{F_+} d, \frac{k_{F_-}}{k_{F_+}}\right) \right] \right\}, \end{aligned} \quad (61)$$

where k_{F_-} and k_{F_+} are Fermi momenta, n_- and n_+ are electron densities of quasiparticle bands $|-\rangle$ and $|+\rangle$, respectively. The HF energy per electron is

$$\varepsilon_{\text{tot}}^{S_2'} = \frac{1}{nA} (E_{\text{kin}} + E_{\text{H}} + E_x^{\text{intra}} + E_x^{\text{inter}}). \quad (62)$$

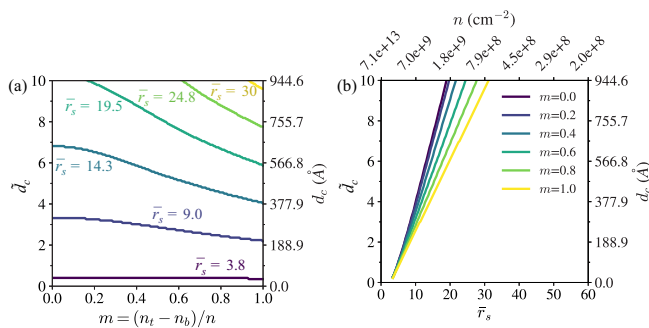


FIG. 7. (a) \tilde{d}_c versus layer polarization m for six values of $\bar{r}_s \in [3.8, 30]$. (b) \tilde{d}_c versus \bar{r}_s for six values of $m \in [0, 1]$. \bar{r}_s is defined by the average layer density using $\bar{r}_s \alpha^* = \sqrt{2/\pi n}$.

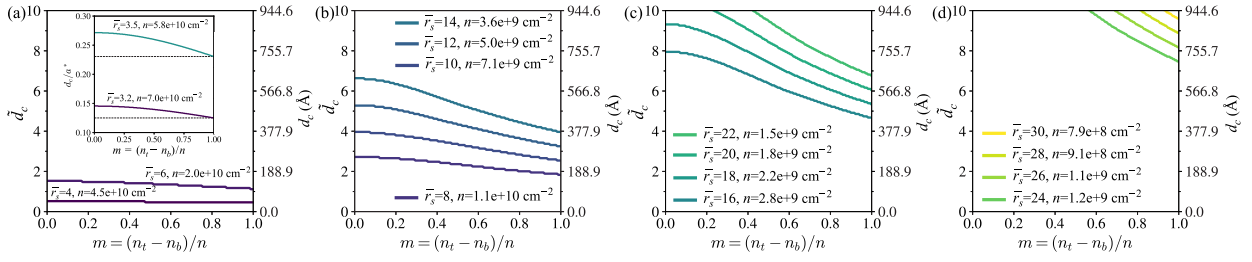


FIG. 8. Same as Fig. 7(a) but with more fixed values of $\bar{r}_s \in [4, 30]$. The inset in (a) shows two smaller \bar{r}_s . At large density, corresponding to small \bar{r}_s , \bar{d}_c exhibits a negligible dependence on m , as expected from our previous analysis in Eq. (53). As $n \rightarrow n_{\max}$ in Eq. (52), \bar{d}_c is independent of m and approaches zero. The black dashed lines in the inset of (a) plot the \bar{d}_c using Eq. (53).

Particularly, when $n_- = n_+ = n/2$, $k_{F_-} = k_{F_+}$, the pseudospin is unpolarized and the energies recover the ones of the S_1 state in Eq. (23).

In Fig. 10, we show $\varepsilon_{\text{tot}}^{S_2^*}$ as a function of pseudospin polarization m_ξ , defined as the ratio of density difference between $|-\rangle$ and $|+\rangle$ eigenstates,

$$m_\xi = \frac{n_- - n_+}{n}. \quad (63)$$

We specifically pick two points in (r_s, \bar{d}) parameter space: one at $r_s = 8, \bar{d} = 1$ in Fig. 10(a) where the ground state is anticipated to be S_2 ($m_\xi = 1$), and the other at $r_s = 8, \bar{d} = 2.8$ in Fig. 10(b) where S_1 state ($m_\xi = 0$) is expected from the phase diagram Fig. 2. In both Figs. 10(a) and 10(b), however, $\varepsilon_{\text{tot}}^{S_2^*}$ is minimized at an intermediate value of m_ξ . This optimal polarization m_ξ^* , at which the energy is minimized, is depicted in Fig. 10(c). m_ξ^* tends to be 1 for large r_s and small \bar{d} , while tends to be 0 for small r_s and large \bar{d} .

In Fig. 11(b) we estimate the critical temperature T_c by taking the difference between the ground-state energy $\varepsilon_{\text{tot}}^G = \min\{\varepsilon_{\text{tot}}^{S_0}, \varepsilon_{\text{tot}}^{S_1}, \varepsilon_{\text{tot}}^{S_2}, \varepsilon_{\text{tot}}^{S_2^*}(m_\xi^*)\}$, and the second lowest energy.

Here $\varepsilon_{\text{tot}}^{S_2^*}(m_\xi^*)$ is the energy of the interlayer coherent state at the optimal pseudospin polarization m_ξ^* . For reference, $\varepsilon_{\text{tot}}^{S_2^*}(m_\xi = 1) = \varepsilon_{\text{tot}}^{S_2}$ and $\varepsilon_{\text{tot}}^{S_2^*}(m_\xi = 0) = \varepsilon_{\text{tot}}^{S_1}$. As a comparison, we show in Fig. 11(a) the T_c by taking the difference between the ground-state energy $\varepsilon_{\text{tot}}^G = \min\{\varepsilon_{\text{tot}}^{S_0}, \varepsilon_{\text{tot}}^{S_1}, \varepsilon_{\text{tot}}^{S_2}\}$ and the second lowest energy. The T_c phase diagram in Fig. 11(b), incorporating pseudospin partially polarized states, yields a higher T_c , up to threefold, than that in Fig. 11(a).

IV. FINITE-TEMPERATURE PHASE DIAGRAMS

In this section, we extend our study to the behavior of interlayer coherence at finite temperatures, by solving for the critical temperature T_c using self-consistent HF approach. We focus on the case for equal layer densities. In Sec. IV A, T_c is determined for the interlayer coherent phase S_2 . In the subsequent Sec. IV B, we broaden the scope of our examination to the exciton condensates in the e-h bilayer. By employing the same range of parameters as those in the e-e bilayer case, we facilitate a direct comparative analysis between the two systems' T_c phase diagrams. This comparative framework not only highlights the unique characteristics of each system, but

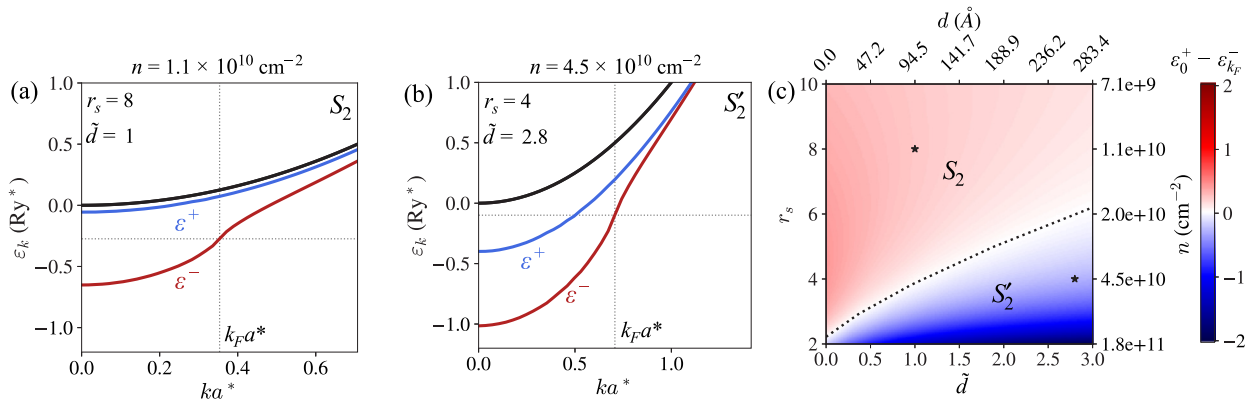


FIG. 9. (a), (b) Interlayer coherent quasiparticle energies in Eq. (59) for equal layer densities. $\varepsilon_{\mathbf{k}}^{1,2}$ are degenerate and represented by black solid lines. $\varepsilon_{\mathbf{k}}^-$ and $\varepsilon_{\mathbf{k}}^+$ are pseudospin-polarized symmetric and antisymmetric states, respectively. (a) $r_s = 8, \bar{d} = 1$, corresponding to $n = 1.1 \times 10^{10} \text{ cm}^{-2}$. (b) $r_s = 4, \bar{d} = 2.8$, corresponding to $n = 4.5 \times 10^{10} \text{ cm}^{-2}$. These two points are marked by stars in the phase diagram in (c). In (a) and (b), the Fermi momentum is denoted by the vertical dotted line and the corresponding Fermi energy is denoted by the horizontal one. We refer to case (a) as stable S_2 phase because only $|-\rangle$ band is occupied, and to (b) as the S_2^* phase in which both quasiparticle bands $|\pm\rangle$ are populated. (c) The phase diagram determined by the energy difference $\varepsilon_0^+ - \varepsilon_{k_F}^-$ as a function of r_s and \bar{d} . The S_2 phase in (c) encompasses a more extensive portion of the parameter space compared to the previously obtained phase diagram in Fig. 2. The dashed line in (c) traces the phase transition boundary.

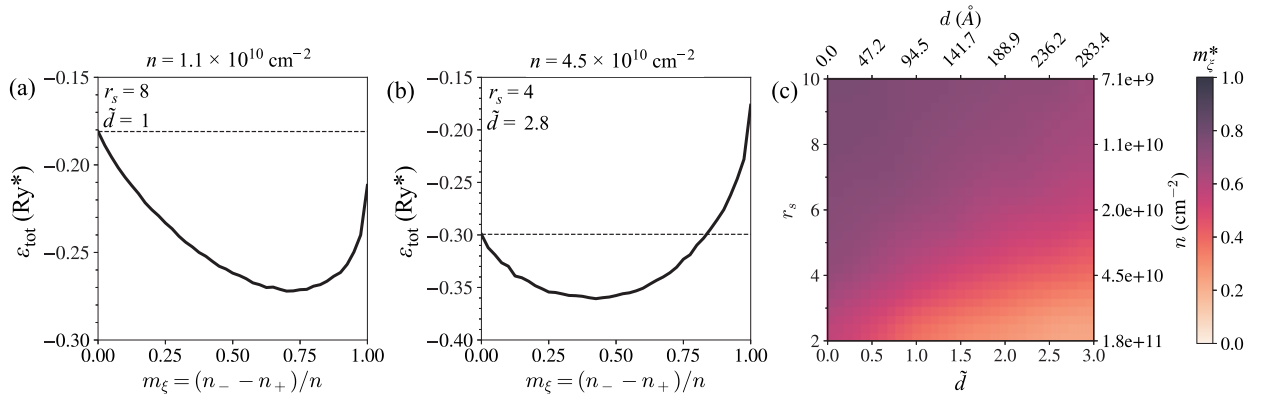


FIG. 10. (a), (b) $\varepsilon_{\text{tot}}^{S_2}$ as a function of the pseudospin polarization m_ξ , at (a) $r_s = 8$, $\tilde{d} = 1$ and (b) $r_s = 4$, $\tilde{d} = 2.8$. The horizontal dotted lines mark the HF energies of the S_1 phase, converging to the same value of $\varepsilon_{\text{tot}}^{S_2}$ at $m_\xi = 0$. In both (a) and (b), $\varepsilon_{\text{tot}}^{S_2}$ is minimized at an intermediate m_ξ . (c) The phase diagram of m_ξ^* versus (r_s, \tilde{d}) , where m_ξ^* is the optimal polarization at which $\varepsilon_{\text{tot}}^{S_2}$ is minimized. m_ξ^* tends to be 1 for large r_s and small \tilde{d} , while tends to be 0 for small r_s and large \tilde{d} .

also underscores the underlying different interacting nature governing their phase transitions at elevated temperatures.

A. T_c of interlayer coherent phase (S_2)

We focus on the majority-spin subspace and ignore the minority spin for the spin-polarized interlayer coherent phase S_2 . To simplify notations, we will therefore ignore the spin superscripts in the following part. With spinor basis $(c_{t\mathbf{k}} \ c_{b\mathbf{k}})^T$, the HF Hamiltonian is

$$\hat{H}_{\text{HF}}^{S_2}(\mathbf{k}) = \begin{pmatrix} \varepsilon_{t\mathbf{k}} & -\Delta_{\mathbf{k}} \\ -\Delta_{\mathbf{k}}^* & \varepsilon_{b\mathbf{k}} \end{pmatrix}, \quad (64)$$

with eigenvectors

$$\begin{pmatrix} +, \mathbf{k} \\ -, \mathbf{k} \end{pmatrix} = \begin{pmatrix} \beta & -\alpha \\ \alpha & \beta \end{pmatrix} \begin{pmatrix} c_{t\uparrow\mathbf{k}} \\ c_{b\uparrow\mathbf{k}} \end{pmatrix} \quad (65)$$

and quasiparticle energies

$$\varepsilon_{\mathbf{k}}^\pm = \frac{1}{2}(\varepsilon_{t\mathbf{k}} + \varepsilon_{b\mathbf{k}}) \pm \sqrt{\xi_{\mathbf{k}}^2 + |\Delta_{\mathbf{k}}|^2}, \quad (66)$$

where

$$\varepsilon_{t\mathbf{k}} = \varepsilon_0(\mathbf{k}) + V_{H,t} + V_{x,t}(\mathbf{k}),$$

$$\varepsilon_{b\mathbf{k}} = \varepsilon_0(\mathbf{k}) + V_{H,b} + V_{x,b}(\mathbf{k}),$$

$$\xi_{\mathbf{k}} = \frac{1}{2}(\varepsilon_{t\mathbf{k}} - \varepsilon_{b\mathbf{k}}). \quad (67)$$

At finite temperatures,

$$V_{H,t} = \frac{2\pi e^2 d}{A\epsilon} \sum_{\mathbf{k}} [\beta^2 f(\varepsilon_{\mathbf{k}}^+) + \alpha^2 f(\varepsilon_{\mathbf{k}}^-)],$$

$$V_{H,b} = \frac{2\pi e^2 d}{A\epsilon} \sum_{\mathbf{k}} [\alpha^2 f(\varepsilon_{\mathbf{k}}^+) + \beta^2 f(\varepsilon_{\mathbf{k}}^-)],$$

$$V_{x,t}(\mathbf{k}) = -\frac{1}{A} \sum_{\mathbf{k}'} V_{\mathbf{k}'-\mathbf{k}}^S [\beta^2 f(\varepsilon_{\mathbf{k}'}^+) + \alpha^2 f(\varepsilon_{\mathbf{k}'}^-)],$$

$$V_{x,b}(\mathbf{k}) = -\frac{1}{A} \sum_{\mathbf{k}'} V_{\mathbf{k}'-\mathbf{k}}^S [\alpha^2 f(\varepsilon_{\mathbf{k}'}^+) + \beta^2 f(\varepsilon_{\mathbf{k}'}^-)],$$

$$\Delta_{\mathbf{k}} = \frac{1}{A} \sum_{\mathbf{k}'} V_{\mathbf{k}'-\mathbf{k}}^D \alpha \beta [f(\varepsilon_{\mathbf{k}'}^-) - f(\varepsilon_{\mathbf{k}'}^+)], \quad (68)$$

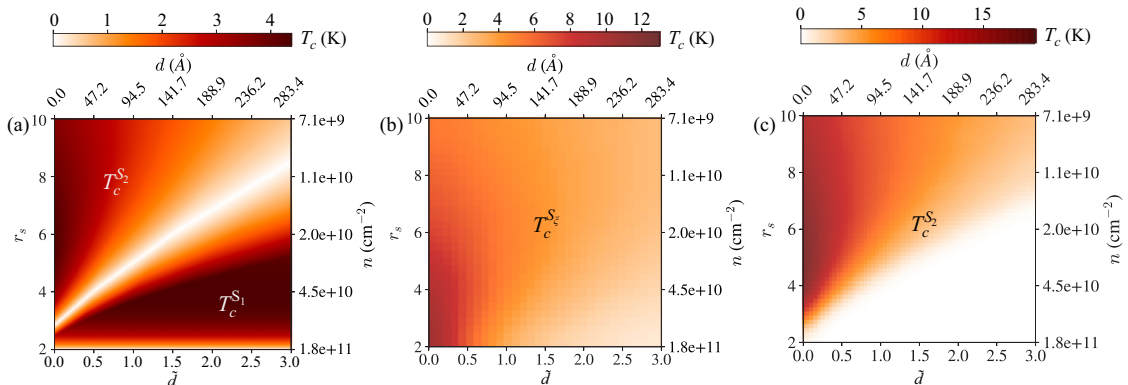


FIG. 11. Critical temperature T_c of the interlayer coherent phase. (a) T_c is calculated by taking the energy difference between the ground state $\varepsilon_{\text{tot}}^G = \min\{\varepsilon_{\text{tot}}^{S_0}, \varepsilon_{\text{tot}}^{S_1}, \varepsilon_{\text{tot}}^{S_2}\}$ and the second lowest-energy state in Sec. III B. (b) T_c is calculated by taking the energy difference between the ground state $\varepsilon_{\text{tot}}^G = \min\{\varepsilon_{\text{tot}}^{S_0}, \varepsilon_{\text{tot}}^{S_1}, \varepsilon_{\text{tot}}^{S_2}, \varepsilon_{\text{tot}}^{S_2}(m_\xi^*)\}$ and the second lowest-energy state in Sec. III D. (c) T_c is calculated by the finite-temperature self-consistent HF using the gaplike equation (70).

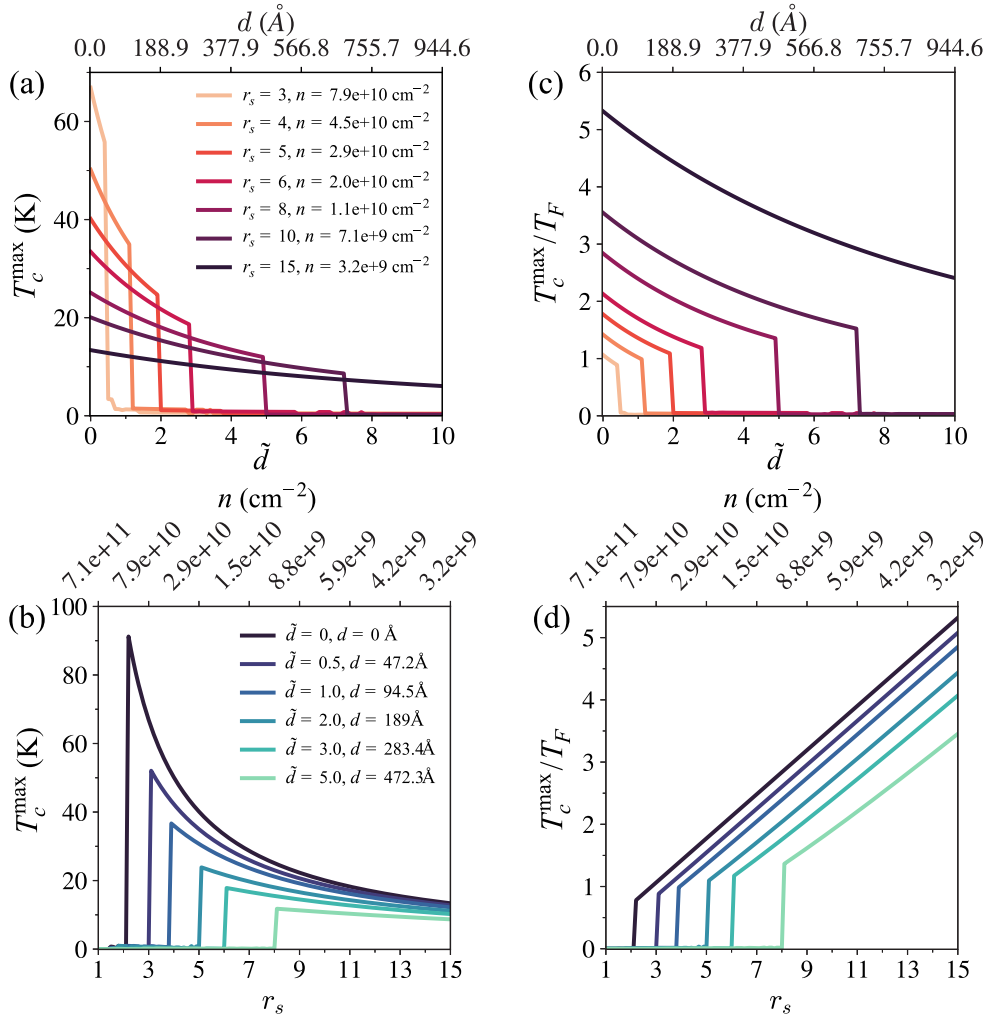


FIG. 12. Critical temperature of the S_2 phase in the e-e bilayer, obtained by zero-temperature self-consistent HF calculations. T_c^{\max} gives the upper-bound critical temperature, determined by $k_B T_c^{\max} = \max_{k \leq k_c} \{\Delta_k\}$, where k_c is the cutoff momentum and chosen to be $k_c = 2k_F$. (a) T_c^{\max} as a function of \tilde{d} for fixed r_s values. (b) T_c^{\max} as a function of r_s for fixed \tilde{d} values. (c) The same as (a) but converted to the dimensionless T_c^{\max}/T_F , sharing the same legend as (a). (d) The same as (b) but converted to the dimensionless T_c^{\max}/T_F , sharing the same legend as (b).

where $f(\varepsilon_{\mathbf{k}}) = [e^{(\varepsilon_{\mathbf{k}} - \mu)/k_B T} + 1]^{-1}$ is the Fermi-Dirac distribution and μ is the chemical potential determined by total density. Both $\xi_{\mathbf{k}}$ and $\Delta_{\mathbf{k}}$, which are momentum-orientation independent, should be solved self-consistently by

$$\begin{aligned} \xi_{\mathbf{k}} &= \frac{\pi e^2}{A\epsilon} \sum_{\mathbf{k}'} \left(d - \frac{1}{|\mathbf{k}' - \mathbf{k}|} \right) \\ &\quad \times [(\alpha^2 - \beta^2)[f(\varepsilon_{\mathbf{k}'}^-) - f(\varepsilon_{\mathbf{k}'}^+)], \\ \Delta_{\mathbf{k}} &= \frac{2\pi e^2}{A\epsilon} \sum_{\mathbf{k}'} \frac{e^{-d|\mathbf{k}' - \mathbf{k}|}}{|\mathbf{k}' - \mathbf{k}|} \alpha\beta [f(\varepsilon_{\mathbf{k}'}^-) - f(\varepsilon_{\mathbf{k}'}^+)]. \end{aligned} \quad (69)$$

For the S_2 phase under our consideration, $\alpha = \beta = 1/\sqrt{2}$, and therefore $\xi_{\mathbf{k}} = 0$. We just need to self-consistently solve the gap equation

$$\Delta_{\mathbf{k}} = \frac{\pi e^2}{A\epsilon} \sum_{\mathbf{k}'} \frac{e^{-d|\mathbf{k}' - \mathbf{k}|}}{|\mathbf{k}' - \mathbf{k}|} [f(\varepsilon_{\mathbf{k}'}^-) - f(\varepsilon_{\mathbf{k}'}^+)]. \quad (70)$$

At $T = 0$, $f(\varepsilon_{\mathbf{k}'}^-) - f(\varepsilon_{\mathbf{k}'}^+) = 1$. We first show the critical temperature obtained from zero-temperature self-consistent

HF calculations, which gives the upper bound T_c^{\max} by $k_B T_c^{\max} = \max_{k \leq k_c} \{\Delta_k\}$, where k_c is the cutoff momentum and chosen to be $k_c = 2k_F$ in the following calculations. We plot T_c^{\max} versus \tilde{d} in Fig. 12(a) and T_c^{\max} versus r_s in Fig. 12(b). There is always a critical \tilde{d}_c ($r_{s,c}$) above (below) which the interlayer coherence vanishes. We convert T_c^{\max} in Kelvin (obtained for GaAs e-e bilayers) to dimensionless T_c^{\max}/T_F in Figs. 12(c) and 12(d), where T_F characterizes the Fermi energy $k_B T_F = \varepsilon_F$.

At finite temperatures, the critical temperature T_c is determined by detecting the transition of $\Delta_{\mathbf{k}}$ from 0 to a finite value: for $T > T_c$, $\Delta_{\mathbf{k}} = 0$; for $T < T_c$, $\Delta_{\mathbf{k}} > 0$. The self-consistently calculated T_c as a function of \tilde{d} and r_s are shown in Fig. 13. As a function of \tilde{d} , T_c at a large r_s shows a power-law decay, qualitatively agreeing with the pseudospin stiffness behavior with respect to the interlayer separation in the quantum Hall bilayer at $\nu = 1$ [58]. Note that any mean-field calculation is crude for large layer separations, where the quantum fluctuations become important. Same as the zero-temperature self-consistent HF calculations, there is a critical \tilde{d}_c ($r_{s,c}$), above (below) which T_c drops to zero,

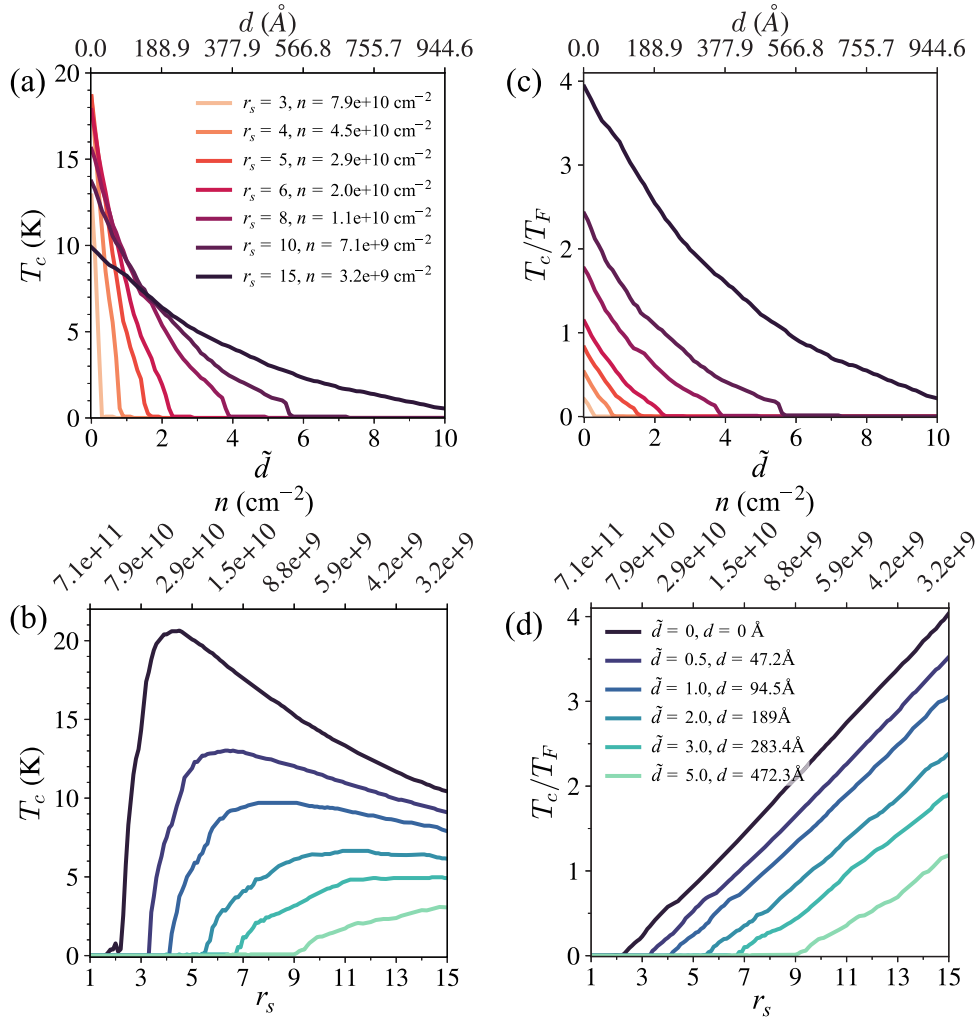


FIG. 13. Critical temperature of the S_2 phase in the e-e bilayer, obtained by finite-temperature self-consistent HF calculations. (a) T_c as a function of \tilde{d} for fixed r_s values. (b) T_c as a function of r_s for fixed \tilde{d} values. (c) The same as (a) but converted to the dimensionless T_c/T_F , sharing the same legend as (a). (d) The same as (b) but converted to the dimensionless T_c/T_F , sharing the same legend as (b).

indicating the phase transition $S_2 \rightarrow S_1$. As a function of r_s shown in Fig. 13(b), after entering the S_2 phase, T_c initially rises quickly then drops slowly with r_s . The behavior of the critical temperature becomes more apparent when expressed in terms of the dimensionless ratio T_c/T_F , which is depicted in Figs. 13(c) and 13(d). Here T_c/T_F decreases with \tilde{d} following a power law but increases almost linearly with r_s .

The complete critical temperature phase diagram, determined by the finite-temperature self-consistent HF calculations, is shown in Fig. 11(c). As expected, T_c is maximized at small \tilde{d} and moderate r_s values. Notably, the phase boundary where T_c vanishes closely mirrors that obtained using the zero-temperature HF energies in Fig. 11(a). T_c under finite-temperature self-consistent HF in Fig. 11(c) is substantially higher, by a factor of 5, compared to the zero-temperature HF energy difference approach in Fig. 11(a). The magnitude of T_c in Fig. 11(c), however, aligns quantitatively with the estimation from zero-temperature HF energy difference approach when incorporating partially polarized pseudospins, in Fig. 11(b). Note that in Fig. 11(c), T_c vanishes for small r_s and large \tilde{d} because we restrict the self-consistent HF to the S_2 phase.

For comparative purposes, we show T_c for the spin-polarized ferromagnetic phase S_1 calculated via finite-temperature self-consistent HF in Appendix C, Fig. 20(a). The S_1 phase is the bilayer 2DEG with two equal Fermi surfaces with Fermi momentum $k_F = \sqrt{2\pi n}$. Therefore, the T_c of S_1 phase is d independent. At $\tilde{d} = 0$, the S_2 phase [shown in the black lines in Figs. 13(b) and 13(d)] is analogous to the S_1 phase, albeit with a single Fermi surface of momentum $k_F = \sqrt{4\pi n}$. Therefore, the trends observed for T_c and T_c/T_F at $\tilde{d} = 0$ in Figs. 13(b) and 13(d) share similar behaviors as those of the S_1 phase in Fig. 20(a), with differences attributable to the number of Fermi surfaces.

B. T_c of exciton condensates in electron-hole bilayer

In this subsection we consider e-h bilayers, on an equal footing with the above-described e-e bilayers, with electrons in one layer and holes in the other layer, forming exciton condensates. This architecture provides a direct comparison with the S_2 phase in e-e bilayers, facilitating a deeper and broader understanding of interlayer coherence phenomena. For an intuitive picture, we categorize the electrons as residing

in the conduction band (top layer) and the holes in the valence band (bottom layer). The spinless HF Hamiltonian is

$$\begin{aligned}\hat{\mathcal{H}}_{\text{HF}} &= \sum_{\mathbf{k}} \begin{pmatrix} c_{c\mathbf{k}}^\dagger & c_{v\mathbf{k}}^\dagger \end{pmatrix} \begin{pmatrix} \varepsilon_{c\mathbf{k}} & -\Delta_{\mathbf{k}} \\ -\Delta_{\mathbf{k}}^* & \varepsilon_{v\mathbf{k}} \end{pmatrix} \begin{pmatrix} c_{c\mathbf{k}} \\ c_{v\mathbf{k}} \end{pmatrix} \\ &= \sum_{\mathbf{k}} \begin{pmatrix} \tilde{\gamma}_{\mathbf{k}}^\dagger & \gamma_{\mathbf{k}}^\dagger \end{pmatrix} \begin{pmatrix} \varepsilon_{\mathbf{k}}^+ & 0 \\ 0 & \varepsilon_{\mathbf{k}}^- \end{pmatrix} \begin{pmatrix} \tilde{\gamma}_{\mathbf{k}} \\ \gamma_{\mathbf{k}} \end{pmatrix},\end{aligned}\quad (71)$$

The quasiparticle operators using the Bogoliubov transformation are

$$\begin{pmatrix} +, \mathbf{k} \\ -, \mathbf{k} \end{pmatrix} \equiv \begin{pmatrix} \tilde{\gamma}_{\mathbf{k}} \\ \gamma_{\mathbf{k}} \end{pmatrix} = \begin{pmatrix} u_{\mathbf{k}} & -v_{\mathbf{k}} \\ v_{\mathbf{k}}^* & u_{\mathbf{k}}^* \end{pmatrix} \begin{pmatrix} c_{c\mathbf{k}} \\ c_{v\mathbf{k}} \end{pmatrix},\quad (72)$$

with quasiparticle energies

$$\varepsilon_{\mathbf{k}}^\pm = \frac{1}{2}(\varepsilon_{c\mathbf{k}} + \varepsilon_{v\mathbf{k}}) \pm \sqrt{\xi_{\mathbf{k}}^2 + |\Delta_{\mathbf{k}}|^2},\quad (73)$$

where

$$\begin{aligned}\varepsilon_{c\mathbf{k}} &= \varepsilon_{c\mathbf{k}}^{(0)} + V_{H,c} + V_{x,c}(\mathbf{k}), \\ \varepsilon_{v\mathbf{k}} &= \varepsilon_{v\mathbf{k}}^{(0)} + V_{H,v} + V_{x,v}(\mathbf{k}), \\ \varepsilon_{c\mathbf{k}}^{(0)} &= \frac{\hbar k^2}{2m^*}, \\ \varepsilon_{v\mathbf{k}}^{(0)} &= -\frac{\hbar k^2}{2m_c^*} - E_g,\end{aligned}\quad (74)$$

and

$$\begin{aligned}\xi_{\mathbf{k}} &= \frac{1}{2}(\varepsilon_{c\mathbf{k}} - \varepsilon_{v\mathbf{k}}), \\ \Delta_{\mathbf{k}} &= \frac{1}{A} \sum_{\mathbf{k}'} V_{\mathbf{k}-\mathbf{k}'}^D \langle c_{v\mathbf{k}'}^\dagger c_{c\mathbf{k}'} \rangle.\end{aligned}\quad (75)$$

E_g is the overlap between conduction and valence bands and is determined by the initial setting of the electron density n_e . Note that we assign different effective masses to conduction and valence bands simply because the divergent negative Fermi sea should be taken into account in m_v^* [68]. The valence band effective mass is renormalized by the exchange interactions of occupied remote band states:

$$\begin{aligned}-\frac{\hbar^2 k^2}{2m_v^*} &= -\frac{\hbar^2 k^2}{2m^*} - \frac{1}{A} \sum_{\mathbf{k}'} V_{\mathbf{k}-\mathbf{k}'}^S \langle c_{v\mathbf{k}'}^\dagger c_{v\mathbf{k}'} \rangle_0 \\ &= -\frac{\hbar^2 k^2}{2m^*} - \frac{1}{A} \sum_{\mathbf{k}'} V_{\mathbf{k}-\mathbf{k}'}^S \rho_{vv}^0(\mathbf{k}'),\end{aligned}\quad (76)$$

where $\rho_{vv}^0(\mathbf{k}') = \langle c_{v\mathbf{k}'}^\dagger c_{v\mathbf{k}'} \rangle_0 = 1$ is the expectation value in the reference state $|\Phi_0\rangle$ that all valence band states are occupied and all conduction band states are empty. We should subtract this reference state expectation in all $\rho_{vv}(\mathbf{k})$ terms, and we denote them as

$$\tilde{\rho}_{vv}(\mathbf{k}) = \rho_{vv}(\mathbf{k}) - \rho_{vv}^0(\mathbf{k}).\quad (77)$$

The Hartree terms in Eq. (75) are

$$\begin{aligned}V_{H,c} &= -V_{H,v} \\ &= \frac{\pi e^2 d}{A\epsilon} \sum_{\mathbf{k}'} (\rho_{cc}(\mathbf{k}') - \tilde{\rho}_{vv}(\mathbf{k}')).\end{aligned}\quad (78)$$

For equal electron and hole densities that we consider here,

$$V_{H,c} = \frac{2\pi e^2 d n_e}{\epsilon},\quad (79)$$

where

$$n_e = \frac{1}{A} \sum_{\mathbf{k}} \rho_{cc}(\mathbf{k})\quad (80)$$

is the electron density. The exchange terms in Eq. (75) are

$$\begin{aligned}V_{x,c} &= -\frac{1}{A} \sum_{\mathbf{k}'} V_{\mathbf{k}-\mathbf{k}'}^S \rho_{cc}(\mathbf{k}'), \\ V_{x,v} &= -\frac{1}{A} \sum_{\mathbf{k}'} V_{\mathbf{k}-\mathbf{k}'}^S \tilde{\rho}_{vv}(\mathbf{k}'), \\ \Delta_{\mathbf{k}} &= \frac{1}{A} \sum_{\mathbf{k}'} V_{\mathbf{k}-\mathbf{k}'}^D \rho_{cv}(\mathbf{k}').\end{aligned}\quad (81)$$

At finite temperatures, the density matrix elements are

$$\begin{aligned}\rho_{cc}(\mathbf{k}) &= \langle c_{c\mathbf{k}}^\dagger c_{c\mathbf{k}} \rangle = |v_{\mathbf{k}}|^2 f(\varepsilon_{\mathbf{k}}^-) + |u_{\mathbf{k}}|^2 f(\varepsilon_{\mathbf{k}}^+), \\ \tilde{\rho}_{vv}(\mathbf{k}) &= \langle c_{v\mathbf{k}}^\dagger c_{v\mathbf{k}} \rangle - 1 = |u_{\mathbf{k}}|^2 f(\varepsilon_{\mathbf{k}}^-) + |v_{\mathbf{k}}|^2 f(\varepsilon_{\mathbf{k}}^+) - 1, \\ \rho_{cv}(\mathbf{k}) &= \langle c_{v\mathbf{k}}^\dagger c_{c\mathbf{k}} \rangle = u_{\mathbf{k}}^* v_{\mathbf{k}} [f(\varepsilon_{\mathbf{k}}^-) - f(\varepsilon_{\mathbf{k}}^+)].\end{aligned}\quad (82)$$

We need to self-consistently solve for

$$\begin{aligned}\xi_{\mathbf{k}} &= \frac{1}{2}(\varepsilon_{c\mathbf{k}}^{(0)} - \varepsilon_{v\mathbf{k}}^{(0)}) + \frac{2\pi e^2 d n_e}{\epsilon} - \frac{\pi e^2}{A\epsilon} \sum_{\mathbf{k}'} \frac{1}{|\mathbf{k}-\mathbf{k}'|} \\ &\quad \times \left[1 - \frac{\xi_{\mathbf{k}'}}{\sqrt{\xi_{\mathbf{k}'}^2 + |\Delta_{\mathbf{k}'}|^2}} \tanh\left(\frac{\sqrt{\xi_{\mathbf{k}'}^2 + |\Delta_{\mathbf{k}'}|^2}}{2k_B T}\right) \right], \\ \Delta_{\mathbf{k}} &= \frac{\pi e^2}{A\epsilon} \sum_{\mathbf{k}'} \frac{e^{-d|\mathbf{k}-\mathbf{k}'|}}{|\mathbf{k}-\mathbf{k}'|} \frac{\Delta_{\mathbf{k}'}}{\sqrt{\xi_{\mathbf{k}'}^2 + |\Delta_{\mathbf{k}'}|^2}} \tanh\left(\frac{\sqrt{\xi_{\mathbf{k}'}^2 + |\Delta_{\mathbf{k}'}|^2}}{2k_B T}\right).\end{aligned}\quad (83)$$

We have used

$$|u_{\mathbf{k}}|^2 = \frac{1}{2} \left(1 + \frac{\xi_{\mathbf{k}}}{\sqrt{\xi_{\mathbf{k}}^2 + |\Delta_{\mathbf{k}}|^2}} \right),\quad (84)$$

$$|v_{\mathbf{k}}|^2 = \frac{1}{2} \left(1 - \frac{\xi_{\mathbf{k}}}{\sqrt{\xi_{\mathbf{k}}^2 + |\Delta_{\mathbf{k}}|^2}} \right),\quad (85)$$

$$u_{\mathbf{k}}^* v_{\mathbf{k}} = \frac{\Delta_{\mathbf{k}}}{2\sqrt{\xi_{\mathbf{k}}^2 + |\Delta_{\mathbf{k}}|^2}},\quad (86)$$

$$f(\varepsilon_{\mathbf{k}}^-) - f(\varepsilon_{\mathbf{k}}^+) = \tanh\left(\frac{\sqrt{\xi_{\mathbf{k}}^2 + |\Delta_{\mathbf{k}}|^2}}{2k_B T}\right).\quad (87)$$

At $T = 0$, $f(\varepsilon_{\mathbf{k}}^-) - f(\varepsilon_{\mathbf{k}}^+) = 1$. We first show the critical temperature obtained from zero-temperature self-consistent HF calculations, which gives the upper bound T_c^{max} by $k_B T_c^{\text{max}} = \max_{k \leq k_c} \{\Delta_k\}$, where k_c is the cutoff momentum and chosen to be $k_c = 4 \text{ nm}^{-1}$ in the following calculations. In Fig. 14(a), we plot T_c^{max} versus \tilde{d} , observing an exponential decay of T_c^{max} with increasing \tilde{d} . As a function of

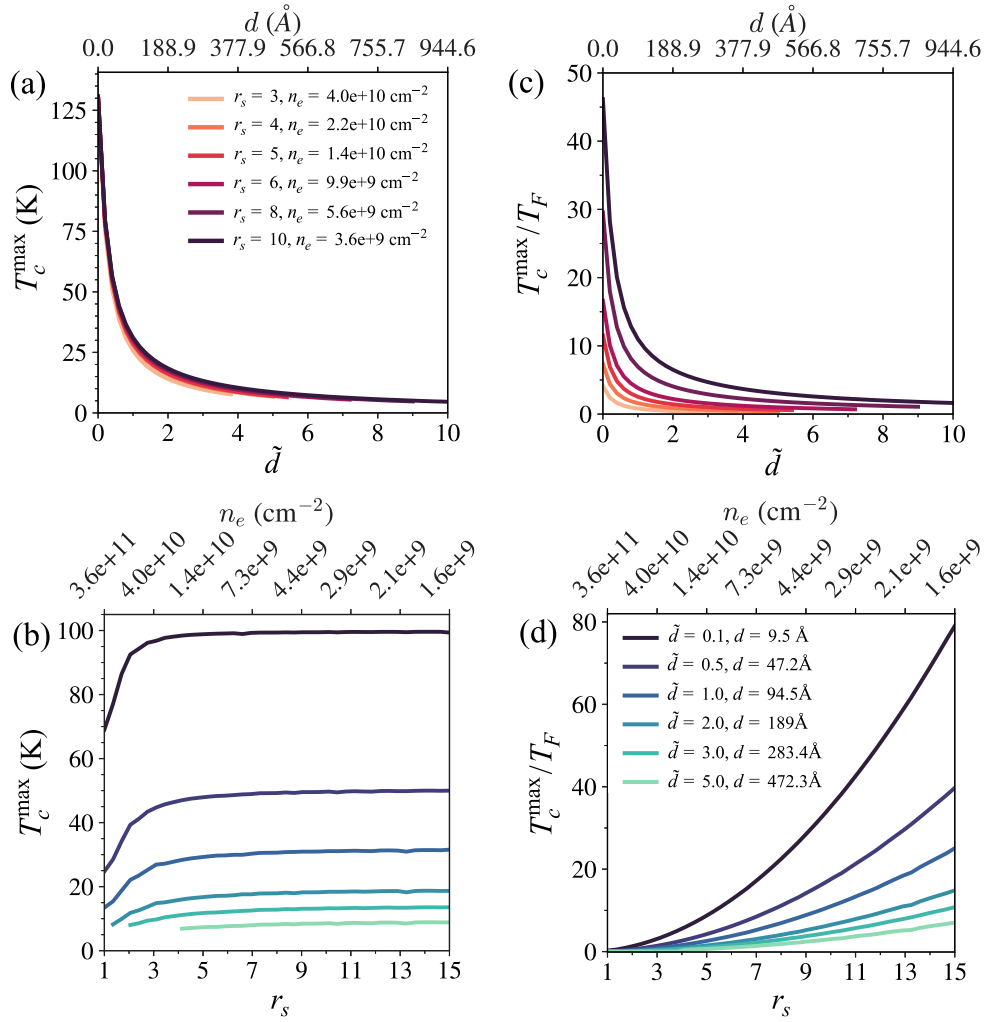


FIG. 14. Critical temperature of exciton condensates in the e-h bilayer. T_c^{\max} is estimated by zero-temperature self-consistent HF calculations, which gives the upper bound T_c^{\max} by $k_B T_c^{\max} = \max_{k \leq k_c} \{\Delta_k\}$, where k_c is the cutoff momentum and chosen to be $k_c = 4 \text{ nm}^{-1}$. (a) T_c^{\max} as a function of \tilde{d} for fixed r_s values. (b) T_c^{\max} as a function of r_s for fixed \tilde{d} values. (c) The same as (a) but converted to the dimensionless T_c^{\max}/T_F , sharing the same legend as (a). (d) The same as (b) but converted to the dimensionless T_c^{\max}/T_F , sharing the same legend as (b).

r_s in Fig. 14(b), T_c^{\max} first rises and then almost stabilizes at higher r_s values. The approximate invariance in T_c^{\max} at large r_s is attributed to the converged exciton pair density and exciton binding energy [23]. We convert T_c^{\max} in Kelvin (for GaAs bilayers) to dimensionless T_c^{\max}/T_F in Figs. 14(c) and 14(d).

Extending to finite temperatures, self-consistent HF calculations reveal T_c trends similar to those at zero temperature. The T_c obtained from finite-temperature calculations are approximately half of those predicted by T_c^{\max} , as depicted in Fig. 15, and is consistent with variational quantum Monte Carlo calculations [69]. Note that quantitative detailed differences between our mean-field study and the Monte Carlo study are attributed to the screening effects absent in our theory. The dashed line in Fig. 15(b) marks the critical temperature of the BKT transition, $T_c^{\text{BKT}} \approx 1.3 \hbar^2 n / 2m^*$, calculated using the converged exciton pair density n at $\tilde{d} = 0.1$. In the BEC limit (large r_s), T_c^{BKT} becomes independent of r_s , due to the converged exciton pair density.

In Fig. 16, we compare order parameters as a function of temperature for e-e and e-h bilayers. Figures 16(a) and 16(d) display the maximum value of Δ_k against the temperature T . For the e-e bilayer, we observe a relatively sharp drop in the order parameter as the temperature increases and approaches the critical value, followed by a more gradual decrease to zero with further temperature increase. In contrast, the e-h bilayer exhibits a more gradual drop in the order parameter with increasing temperature, transitioning abruptly to zero as it approaches the critical temperature. This contrasting behavior between e-e and e-h bilayers is further elucidated in Figs. 16(b) and 16(e), where both the order parameter and temperature are presented in dimensionless form. Here, the fluctuations in the e-e bilayer are noticeably larger than those in the e-h bilayer, reflecting a closer resemblance to magnetic transition behaviors in the e-e bilayer. Additionally, Figs. 16(c) and 16(f) trace the momentum k at which the order parameter Δ_k reaches its maximum. In the e-e bilayer, Δ_k maximum consistently occurs at $k = 0$ for temperatures

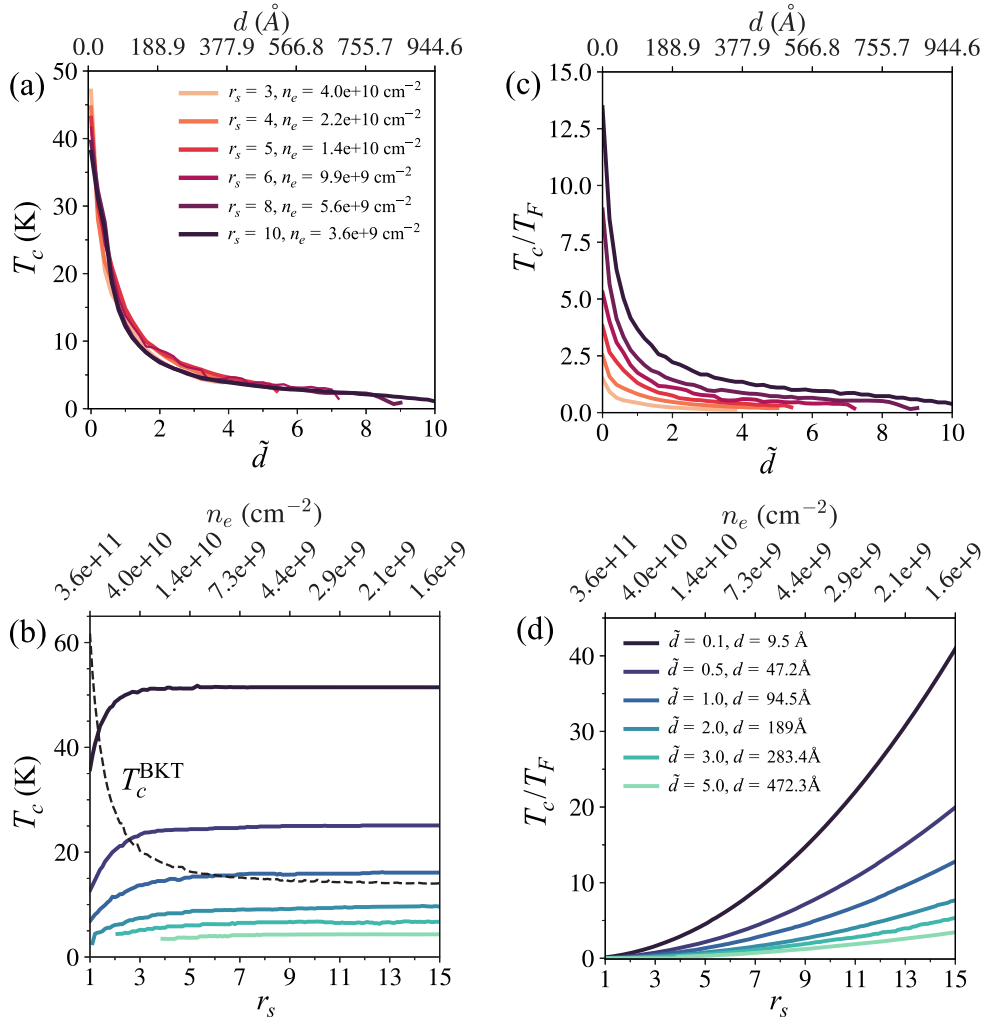


FIG. 15. Critical temperature T_c of exciton condensates in the e-h bilayer. T_c is determined by the finite-temperature self-consistent HF calculations. (a) T_c as a function of \tilde{d} for fixed r_s values. (b) T_c as a function of r_s for fixed \tilde{d} values. (c) The same as (a) but converted to the dimensionless T_c/T_F , sharing the same legend as (a). (d) The same as (b) but converted to the dimensionless T_c/T_F , sharing the same legend as (b). The dashed line in (b) marks the critical temperature of the BKT transition, $T_c^{\text{BKT}} \approx 1.3\hbar^2 n/2m^*$, at $\tilde{d} = 0.1$, where n is the converged exciton pair density.

below T_c , whereas in the e-h bilayer, Δ_k is maximized at a finite momentum. Notably, this finite momentum diminishes towards zero as r_s increases [23,24].

We end our discussion with a side-by-side comparison of the T_c behaviors in e-e and e-h bilayers in Fig. 17. The main difference between XY pseudospin ferromagnetism in e-e bilayers and exciton condensates in e-h bilayers lies in their dependence of interlayer coherence on r_s . The e-e bilayer necessitates a minimum or critical r_s for the existence of its coherent phase, with U(1) symmetry breaking only manifesting above a critical $r_{s,c}$. By contrast, the e-h bilayer exhibits exciton condensation for all r_s values at zero temperature. However, this difference is not practically significant as exciton condensates in e-h bilayers exhibit exponentially low T_c for small r_s values, rendering them unobservable in this range. Despite similarities in their gaplike equations [Eqs. (70) and (83)], e-e and e-h bilayers differ in two key aspects. First, e-h bilayers always include a Hartree term proportional to the layer separation d , a term that is absent in e-e bilayers with

equal layer densities. Second, at charge neutrality in e-h bilayers, where electron and hole densities are equal, the Fermi level invariably sits at the midpoint of the two quasiparticle bands. This results in the tangent term in the gap equation. In contrast, in e-e bilayers, the term $(\varepsilon_{\mathbf{k}^-} + \varepsilon_{\mathbf{k}^+})$ in Eq. (66) varies with k , meaning that $f(\varepsilon_{\mathbf{k}^-}) - f(\varepsilon_{\mathbf{k}^+})$ in Eq. (70) cannot be simplified to the tangent function. This comparison highlights the distinct thermal characteristics, underscoring the differences in the formation of coherent phases in these two analogous but distinct bilayer configurations.

V. EFFECTS OF INTERLAYER TUNNELING

We focus in this section on the impact of interlayer tunneling on the XY pseudospin ferromagnetic transition in e-e bilayers, which is analogous to the influence of an in-plane magnetic field in ferromagnetic spin systems.

The HF Hamiltonian (64) is slightly modified with an interlayer tunneling t , acting as an effective magnetic field in the

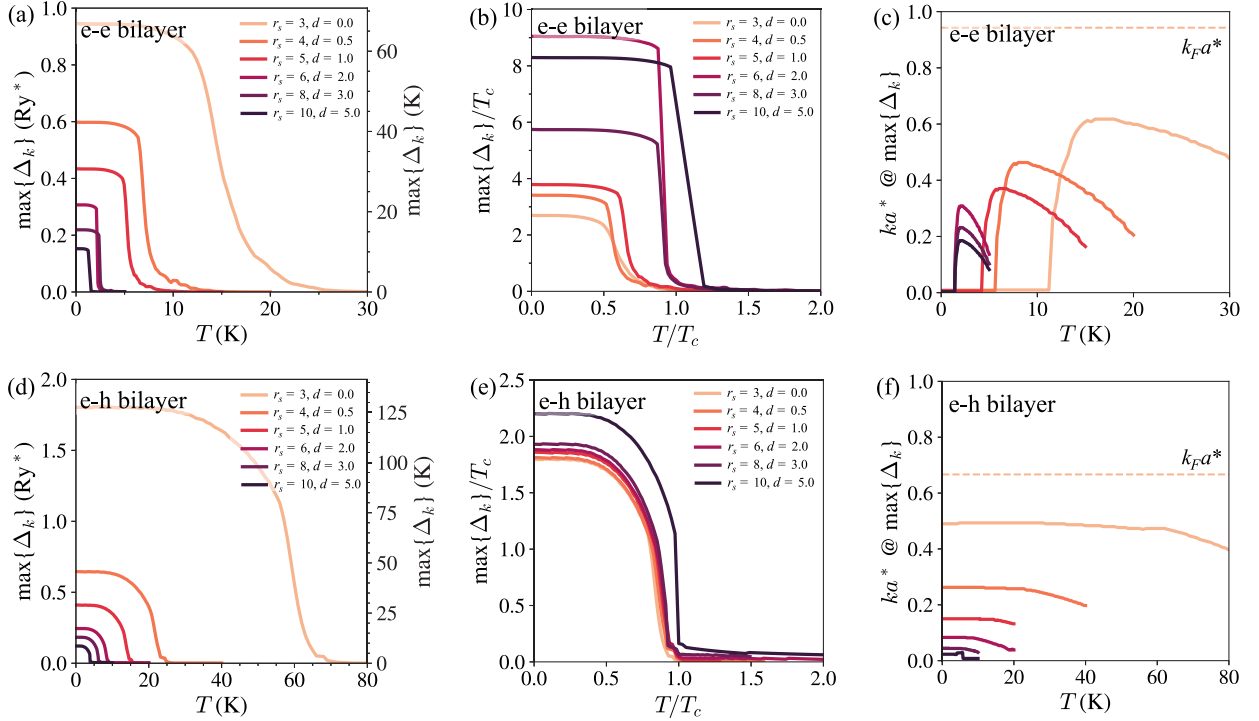


FIG. 16. A side-by-side comparison of the interlayer coherence order parameter $\max\{\Delta_k\}$ as a function of temperature in e-e (a)–(c) and e-h (d)–(f) bilayers. (a), (d) The order parameter $\max\{\Delta_k\}$ versus temperature T . (b), (e) Same as (a) and (d) but both $\max\{\Delta_k\}$ and T are converted to be dimensionless. The fluctuations in the e-e bilayer are larger than in the e-h bilayer because the e-e bilayer aligns more like the magnetic transition. (c), (f) The momentum k , at which the order parameter Δ_k is the maximum, versus the temperature. For the e-e bilayer, maximum Δ_k is always at $k = 0$ for $T < T_c$, while for the e-h bilayer, Δ_k is maximized at a finite momentum. This finite momentum decreases to zero as r_s increases [23,24].

x direction:

$$\hat{H}_{\text{HF}}^{S_2}(\mathbf{k}) = \begin{pmatrix} \varepsilon_{t\mathbf{k}} & -\Delta_{\mathbf{k}} + t \\ -\Delta_{\mathbf{k}}^* + t & \varepsilon_{b\mathbf{k}} \end{pmatrix}. \quad (88)$$

The quasiparticle energies become

$$\varepsilon_{\mathbf{k}}^{\pm} = \frac{1}{2}(\varepsilon_{t\mathbf{k}} + \varepsilon_{b\mathbf{k}}) \pm \sqrt{\xi_{\mathbf{k}}^2 + |\Delta_{\mathbf{k}} - t|^2}, \quad (89)$$

and the gap equation (68) is modified in terms of Fermi-Dirac distribution.

We investigate the effects of a small interlayer tunneling t on the averaged spontaneous gap $\bar{\Delta}_k = \sum_{k \in [0, k_c]} \Delta_k / N_k$, where N_k is the number of k points along $\mathbf{k} = k\hat{k}_x$ and $k \in [0, k_c]$, $k_c = 2k_F$ is the cutoff momentum. Figure 18(a) plots $\bar{\Delta}_k$ versus r_s at fixed $\bar{d} = 1$ and temperature $T = 1$ K, and Fig. 18(b) plots $\bar{\Delta}_k$ versus \bar{d} at fixed $r_s = 4$ and $T = 1$ K. The jumps in $\bar{\Delta}_k$ at critical r_s and \bar{d} indicate the transition exactly as what happens for a ferromagnetic transition in a magnetic field. As expected, the interlayer tunneling indeed suppresses the spontaneous ferromagnetic ordering. This manifests as a shift in the critical r_s to higher values and the critical \bar{d} to lower values, indicating a trend towards requiring a stronger coupling. In the presence of the interlayer tunneling t , the interlayer coherence transition becomes a crossover as the U(1) symmetry is explicitly broken by t , which in the pseudospin language is simply an applied magnetic field in the easy-plane defining the magnetization direction.

VI. CONCLUSION

In this paper, we carry out a comprehensive HF study of XY pseudospin ferromagnetism in zero-field e-e bilayers, and compare it with exciton condensation superfluid in zero-field e-h bilayers, for parabolic bands and long-range Coulomb interactions.

At zero temperature, the phase diagram of e-e bilayers is determined by the HF energy. In e-e bilayers with equal layer densities, the interlayer coherent phase with pseudospin ordered in the xy plane is the stable ground state at lower electron densities (larger r_s) and reduced interlayer separation d . There is, however, always a critical r_s value for the interlayer coherence phase transition, and the system is a pseudospin paramagnet below this d -dependent critical r_s . When layer densities are unequal, we find that the critical layer separation d_c , beyond which interlayer coherence vanishes, decreases with increasing layer density imbalance, but remains present even under complete layer polarization. This layer polarization can be conceptualized as a pseudospin response to an effective magnetic field applied along the z direction. Our results illustrate that, despite a strong effective magnetic field polarizing the pseudospin completely in the z direction, the exchange-driven XY pseudospin ferromagnetic transition remains little affected.

At finite temperatures, we calculate the critical temperature T_c using self-consistent HF theory. We find that T_c for XY pseudospin ferromagnetism in e-e bilayers is approximately

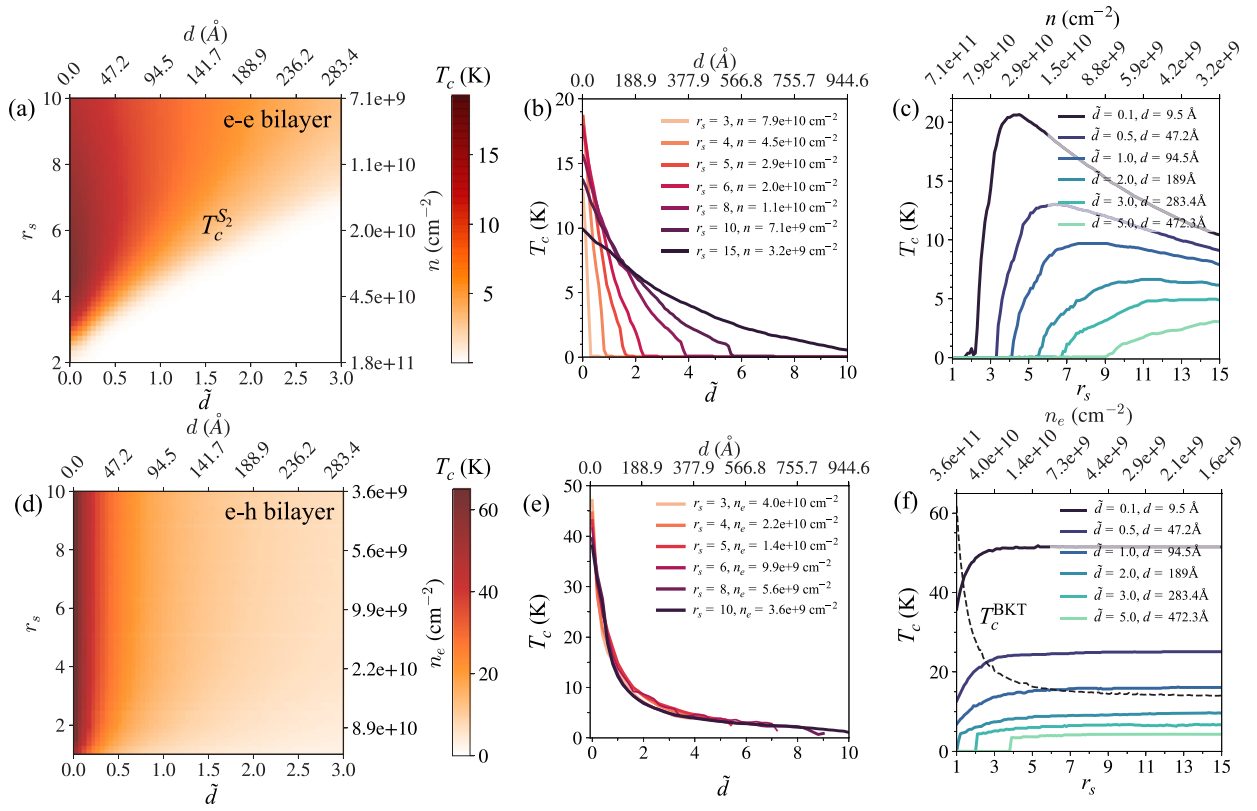


FIG. 17. A side-by-side comparison of the T_c behaviors in e-e (a)–(c) and e-h bilayer (d)–(f) systems. The main difference between the e-e bilayer (XY pseudospin ferromagnet) and the e-h bilayer (exciton condensates) is that the former necessitates a minimum r_s value for its existence with the U(1) symmetry being broken only above a critical $r_{s,c}$, while the latter occurs for all r_s at $T = 0$. This is, however, not a practical difference because the e-h bilayer exciton condensates have exponentially low T_c for small r_s and, therefore, it is unobservable for small r_s any way.

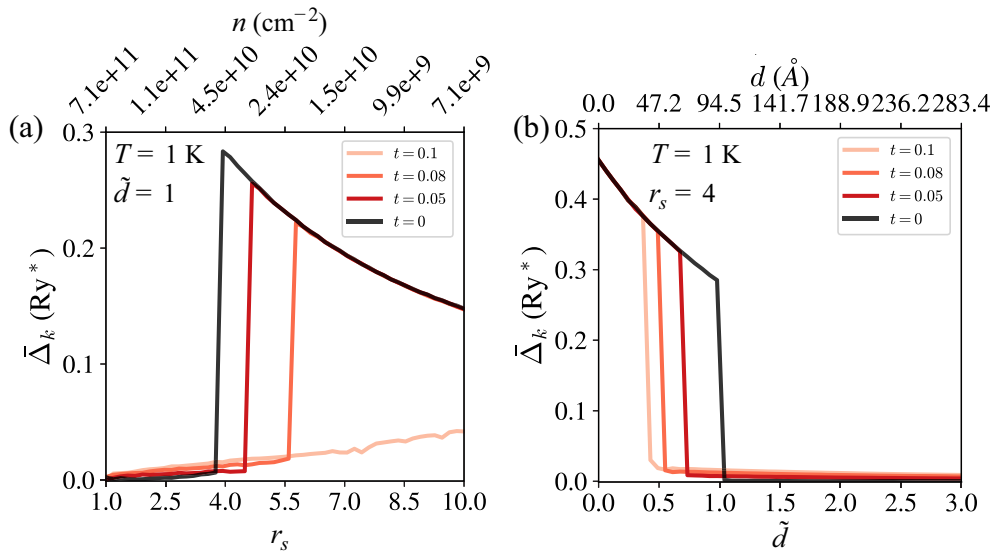


FIG. 18. Effects of interlayer tunneling t on the averaged spontaneous order parameter $\bar{\Delta}_k = \sum_{k \in [0, k_c]} \Delta_k / N_k$, where N_k is the number of k points along $\mathbf{k} = k\hat{k}_x$ and $k \in [0, k_c]$, $k_c = 2k_F$ is the cutoff momentum. Note that even $\bar{\Delta}_k = 0$, two layers are still coherent, even though not spontaneously, because of the finite tunneling t . (a) $\bar{\Delta}_k$ versus r_s at fixed $\tilde{d} = 1$ and $T = 1$ K. (b) $\bar{\Delta}_k$ versus \tilde{d} at fixed $r_s = 4$ and $T = 1$ K. The jumps in $\bar{\Delta}_k$ at critical r_s and \tilde{d} indicate the transition exactly as what happens for a ferromagnetic transition in a magnetic field. In the presence of the interlayer tunneling t , the interlayer coherence transition becomes a crossover as the U(1) symmetry is explicitly broken by t , which in the pseudospin language is simply an applied magnetic field in the easy-plane defining the magnetization direction.

one-third of that for exciton condensates in e-h bilayers, indicating a comparatively weaker interlayer coherence in e-e bilayers. Fluctuations are larger in e-e bilayers because the phase transition aligns more closely to the magnetic transition.

Additionally, we evaluate the influence of weak interlayer tunneling on the interlayer coherence order parameter in e-e bilayers, mimicking the effects of an in-plane magnetic field on XY pseudospin ferromagnetism. In the presence of interlayer tunneling t , the interlayer coherence transition in e-e bilayers becomes a crossover, as the U(1) symmetry is explicitly broken by t .

A notable distinction between XY pseudospin ferromagnetism in e-e bilayers and exciton condensates in e-h bilayers is that the former requires a minimum r_s value for its existence, with U(1) symmetry breaking only above a critical r_s while the latter forms for any r_s at zero temperature. Practically, however, this difference is irrelevant because of the exponentially low T_c for exciton condensates at small r_s values, rendering them unobservable at high densities (i.e., the resultant T_c is exponentially small although finite). The fact that there is no critical density or equivalently no critical layer separation for the exciton condensation in bilayers was revealed in a quantum Hall bilayer experiment with the finding that strong interlayer e-h correlations exist even above the putative transition point showing the transition might be a fast BEC-BCS crossover and not a phase transition [70]. Both XY ferromagnetism and exciton condensates undergo finite-temperature BKT transitions and fall into the same universality class of phase transitions. We emphasize that, unlike in quantum Hall bilayers with the Landau-level filling being $\frac{1}{2}$ in each layer, the interlayer coherence phenomenon is physically very different in the zero-field e-e and e-h bilayers. In the former case, the phenomenon is an XY pseudospin ferromagnetism problem whereas in the latter case, it is an interlayer excitonic condensation superfluid problem. It just so happens that for quantum Hall bilayers, with the exact particle-hole symmetry for half-filled Landau levels, these two descriptions are precisely equivalent, but no such equivalence applies to the zero-field cases considered in this work, where the exact particle-hole symmetry does not apply. For quantum Hall bilayers, the existence or not of an interlayer separation tuned quantum phase transition between interlayer coherent (small separation) and incoherent (large separation) phases has been much discussed in the literature for more than 30 years using many different theoretical approaches [52,71–75]. We believe, based on our current work, that there is no zero-temperature quantum phase transition in quantum Hall bilayers between interlayer coherent and incoherent phases as a function of layer separation (except at the trivial limit of infinite separation), and there is only a crossover between the strongly coupled BEC excitonic condensate at small separation to a weakly coupled BCS excitonic condensate at large separation. Of course, the T_c for the BCS phase being exponentially small and the system behaves like as if there is a phase transition around the crossover regime.

We mention that for very large r_s , each individual 2D layer would undergo a transition to a Wigner crystal phase (which is beyond the scope of our HF theory) breaking the translational invariance in each layer, but maintaining interlayer coherence, and such an interlayer-coherent intralayer Wigner

crystal breaks both interlayer U(1) symmetry and intralayer translational symmetry, and is therefore a supersolid. Similar physics applies also for the e-h bilayers, where the large r_s intralayer translational invariance breaking phase is an exciton crystal with the two layers being interlayer coherent breaking the interlayer U(1) symmetry, leading to an excitonic supersolid [36,65,76].

Although this work lays the groundwork in understanding the differences in interlayer coherence between e-e and e-h bilayers by studying the simple 2DEG model, more complex 2D materials may exhibit richer phenomena. The interlayer coherence physics in these complex systems could be further altered by the band structure, topology, and screening effects. The study of exciton condensates has been extensive in various bilayer systems, including recent graphene-based [50] and transition-metal-dichalcogenide-based bilayers [26], as well as in double-moiré superlattices. There is growing interest in exploring e-e pairing in these systems and its interplay with superconductivity. We will leave these investigations for future study. We just mention in the passing that the well-established phenomena of canted antiferromagnetism in quantum Hall bilayer systems is an example of the interplay among interlayer coherence, spin physics, and interlayer tunneling in filled Landau levels [77–87].

Finally, we briefly discuss the experimental implications of interlayer coherence in zero-field e-h and e-e bilayers. It has been relatively clear that exciton BEC in quantum Hall bilayers is identifiable through specific transport measurements, such as quantized Hall drag resistance in the Coulomb drag geometry, vanishing longitudinal and Hall resistances in the counterflow geometry [31,32,37,88–90], and interlayer tunneling conductance anomalies [91–95]. Identifying exciton condensates in zero-field e-h bilayers remains challenging, though some experiments have come close [15,26,50,96,97]. Transport signatures for a diagnostic of exciton condensates in e-h bilayers include the Coulomb drag and counterflow resistances, and the in-plane Josephson effect. For e-e bilayers, probing the XY pseudospin ferromagnetic metal might be feasible through transport measurements like interlayer tunneling in the presence of an in-plane magnetic field [98–100] and the pseudospin transfer torque [101]. In particular, we predict a giant interaction-induced enhancement of the interlayer tunneling conductance peak in the interlayer coherent phase of e-e bilayers even if the noninteracting system has vanishing interlayer tunneling amplitude. This giant interlayer tunnel resonance would be tunable by changing the layer density and will vanish above a critical density since the interlayer coherence in e-e bilayers can only happen above a critical r_s value. In addition, another experimental approach to observe the spontaneous symmetry-broken interlayer coherent phase could be studying the collective modes of the system, which should manifest the Goldstone mode in the symmetry-broken phase [60], and only regular plasmons in the normal bilayers. Thus, the collective modes of the system should differ for $T < T_c$ and $T > T_c$, with the former showing only one Goldstone mode, but the latter showing both acoustic and optical plasmons of bilayers [102,103]. One issue here is that the Goldstone mode is likely to have a $q^{1/2}$ long-wavelength dispersion (rather than being linear in momentum) because of the 2D analog of the Anderson-Higgs mechanism [104].

Our specific predictions in this work on the dependence of the interlayer coherent phase on the layer density imbalance and/or weak interlayer tunneling should be a useful guide for experimental explorations of the predicted bilayer coherence. The fact that the corresponding transition has been extensively experimentally studied in quantum Hall bilayers, where the XY pseudospin ferromagnet and the exciton superfluid become the same, gives considerable hope that both XY pseudospin ferromagnetism and exciton superfluid condensation will soon be experimentally observed at zero magnetic field in high-quality bilayer systems.

Lastly, we comment on the limitations of the HF mean-field theory. Because of its lack of dynamical screening effects and fluctuations, the HF theory is not a quantitatively accurate method to predict the symmetry-broken ground state, and it overestimates T_c of the phase transition at finite temperatures. However, the HF approximation should always provide a qualitatively accurate phase diagram since it is a mean-field theory using realistic (i.e., Coulomb in our case) interactions. The HF mean-field theory is used extensively in the literature to obtain the quantum phase diagram of electronic materials and is always the first theory to provide a guide to experiments. In addition, our HF theory in predicting the pseudospin phase transitions is proved to be accurate on the mean-field level, as demonstrated in a parallel study using a mean-field self-consistent iterative approach [105]. In the single-layer 2DEG, the spontaneous spin polarization actually occurs at a much larger critical r_s value than the Bloch transition $r_{s,B} \sim 2$ if correlations, which are absent in the HF theory, are included. Given that the pseudospin-polarized (or pseudospin ferromagnetic) phase predicted in our work is a direct result of the interlayer exchange interaction, the pseudospin-polarized phase will also be suppressed by correlations. Therefore, we should expect all the pseudospin phase transitions predicted in our phase diagrams occur at larger r_s and smaller d . But, we see no reason for our calculated phase diagram to be qualitatively incorrect although the symmetry-broken phases are often overestimated in the HF theory.

Finally, we mention that our work is directly applicable to 2D GaAs bilayers (as emphasized by all our figures showing results for GaAs system parameters) where the 2D Fermi surface is not multiply connected, and is in general isotropic and parabolic. For more complicated 2D Fermi surfaces (e.g., transition metal dichalcogenide layers, moiré materials, multi-layer graphene systems), our work would remain qualitatively, but not quantitatively, valid since symmetry-breaking transitions are driven by exchange interactions which always dominate the kinetic energy at low enough densities in Coulomb coupled systems independent of the Fermi-surface details.

ACKNOWLEDGMENT

This work is supported by the Laboratory for Physical Sciences.

APPENDIX A: SUMMARY OF USEFUL SUMMATIONS AND INTEGRALS

We summarize some useful summations and integrals which are frequently used in the equations in the main

text:

$$\sum_{k \leq k_F} = \frac{A}{4\pi} k_F^2, \quad (\text{A1})$$

$$\sum_{k \leq k_F} k^2 = \frac{A}{8\pi} k_F^4, \quad (\text{A2})$$

$$\begin{aligned} \sum_{k, k' \leq k_F} \frac{1}{|\mathbf{k} - \mathbf{k}'|} &= \frac{A}{(2\pi)^2} \sum_{k \leq k_F} \int_{k' \leq k_F} d^2\mathbf{k}' \frac{1}{|\mathbf{k} - \mathbf{k}'|} \\ &= \frac{A}{(2\pi)^2} \sum_{k \leq k_F} \int_0^{k_F} dk' k' \\ &\quad \times \int_0^{2\pi} \frac{d\theta}{\sqrt{(k')^2 + k^2 - 2kk' \cos \theta}} \\ &= \frac{A}{(2\pi)^2} \sum_{k \leq k_F} 4k_F E\left(\frac{k}{k_F}\right) \\ &= \frac{A^2 k_F^3}{2\pi^3} \int_0^1 dx x E(x) \\ &= \frac{A^2 k_F^3}{3\pi^3}, \end{aligned} \quad (\text{A3})$$

$$\begin{aligned} \sum_{k' \leq k_F} \frac{1}{|\mathbf{k} - \mathbf{k}'|} &= \frac{A}{(2\pi)^2} \int_0^{k_F} dk' k' \int_0^{2\pi} \\ &\quad \times \frac{d\theta}{\sqrt{(k')^2 + k^2 - 2kk' \cos \theta}} \\ &= \frac{A}{\pi^2} k_F f_{2D}\left(\frac{k}{k_F}\right), \end{aligned} \quad (\text{A4})$$

$$\begin{aligned} \sum_{k, k' \leq k_F} \frac{e^{-|\mathbf{k} - \mathbf{k}'|d}}{|\mathbf{k} - \mathbf{k}'|} &= \frac{A^2}{(2\pi)^3} \int_0^{k_F} dk k \int_0^{k_F} dk' k' \\ &\quad \times \int_0^{2\pi} d\theta \frac{e^{-d\sqrt{(k')^2 + k^2 - 2kk' \cos \theta}}}{\sqrt{(k')^2 + k^2 - 2kk' \cos \theta}} \\ &= \frac{A^2 k_F^3}{(2\pi)^3} \int_0^1 dx x \\ &\quad \times \int_0^1 dy y \int_0^{2\pi} d\theta \frac{e^{-k_F d \sqrt{x^2 + y^2 - 2xy \cos \theta}}}{\sqrt{x^2 + y^2 - 2xy \cos \theta}} \\ &= \frac{A^2 k_F^3}{(2\pi)^3} J(k_F d), \end{aligned} \quad (\text{A5})$$

$$\begin{aligned} \sum_{k' \leq k_F} \frac{e^{-|\mathbf{k} - \mathbf{k}'|d}}{|\mathbf{k} - \mathbf{k}'|} &= \frac{A}{(2\pi)^2} \int_0^{k_F} dk' k' \int_0^{2\pi} \\ &\quad \times d\theta \frac{e^{-d\sqrt{(k')^2 + k^2 - 2k'k \cos \theta}}}{\sqrt{(k')^2 + k^2 - 2k'k \cos \theta}} \\ &= \frac{Ak_F}{(2\pi)^2} \int_0^1 dy y \int_0^{2\pi} \\ &\quad \times d\theta \frac{e^{-k_F d \sqrt{x^2 + y^2 - 2xy \cos \theta}}}{\sqrt{x^2 + y^2 - 2xy \cos \theta}} \\ &= \frac{Ak_F}{(2\pi)^2} I(x, k_F d), \end{aligned} \quad (\text{A6})$$

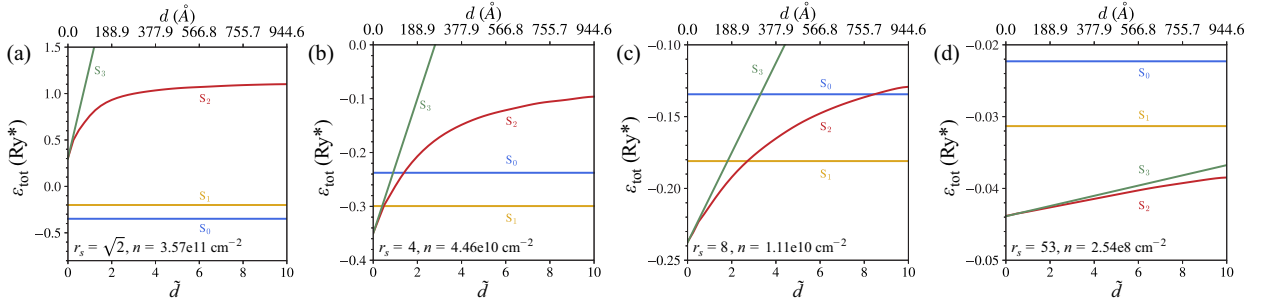


FIG. 19. HF energies as a function of layer distance \tilde{d} for (a) $r_s = \sqrt{2}$, (b) $r_s = 4$, (c) $r_s = 8$, and (d) $r_s = 53$. Dimensionless r_s and \tilde{d} are also converted to density n in units of cm^{-2} and d in units of Å , using GaAs quantum well parameters.

where

$$f_{2D}(x) = \begin{cases} E(x), & x \leq 1 \\ x[E(\frac{1}{x}) - (1 - \frac{1}{x^2})K(\frac{1}{x})], & x \geq 1 \end{cases} \quad (\text{A7})$$

$K(x)$ and $E(x)$ are the complete elliptic integral of the first and the second kind, respectively. $E(x)$ can be expressed as a power series

$$E(x) = \frac{\pi}{2} \sum_{n=0}^{\infty} \left(\frac{(2n)!}{2^{2n}(n!)^2} \right)^2 \frac{x^{2n}}{1-2n}, \quad (\text{A8})$$

and the integration

$$\begin{aligned} \int_0^1 dx x E(x) &= \frac{\pi}{2} \sum_{n=0}^{\infty} \left(\frac{(2n)!}{2^{2n}(n!)^2} \right)^2 \frac{1}{2(n+1)(1-2n)} \\ &= \frac{2}{3}. \end{aligned} \quad (\text{A9})$$

The triple integral $J(k_F d)$,

$$J(k_F d) = \int_0^1 dx x \int_0^1 dy y \int_0^{2\pi} d\theta \frac{e^{-k_F d \sqrt{x^2+y^2-2xy \cos \theta}}}{\sqrt{x^2+y^2-2xy \cos \theta}}, \quad (\text{A10})$$

and the integral

$$I(x, k_F d) = \int_0^1 dy y \int_0^{2\pi} d\theta \frac{e^{-k_F d \sqrt{x^2+y^2-2xy \cos \theta}}}{\sqrt{x^2+y^2-2xy \cos \theta}} \quad (\text{A11})$$

should be evaluated numerically.

APPENDIX B: HF ENERGIES OF THE FOUR COMPETING STATES

In Fig. 19, we show HF energies for competing ground states S_0 , S_1 , S_2 , and S_3 as a function of layer distance \tilde{d} for specific r_s values. The S_2 phase always has a lower energy than the S_3 phase except at $\tilde{d} = 0$.

APPENDIX C: T_c OF THE SPIN-POLARIZED BUT PSEUDOSPIN-UNPOLARIZED PHASE (S_1)

To compare with the T_c of bilayer 2DEG S_1 phase in Sec. III A 2 and in Figs. 13(e) and 13(f), we show T_c of the spin-polarized phase in single 2DEG and single 3DEG.

1. 2DEG

For the spin-polarized phase, the eigenenergy of the majority spin is

$$\varepsilon_{\mathbf{k}} = \varepsilon_0(\mathbf{k}) + V_x(\mathbf{k}), \quad (\text{C1})$$

where

$$\begin{aligned} \varepsilon_0(\mathbf{k}) &= \frac{\hbar^2 k^2}{2m}, \\ V_x(\mathbf{k}) &= -\frac{1}{A} \sum_{\mathbf{k}'} \frac{2\pi e^2}{\epsilon |\mathbf{k} - \mathbf{k}'|} f(\varepsilon_{\mathbf{k}'}). \end{aligned} \quad (\text{C2})$$

The occupied minority-spin state has energy $\varepsilon_0(\mathbf{k})$. At $T = 0$, the Fermi-Dirac distribution $f(\varepsilon_{\mathbf{k}})$ is the step function, and

$$V_x(\mathbf{k}) = -\frac{4a^*}{\pi} k_F E\left(\frac{k}{k_F}\right), \quad (\text{C3})$$

where Fermi momentum $k_F = \sqrt{2\pi n}$. T_c of the 2DEG spin-polarized state, calculated by finite-temperature SCHF, is shown in Fig. 20(b).

2. 3DEG

For the 3DEG, the eigenenergy of the majority spin is

$$\varepsilon_{\mathbf{k}} = \varepsilon_0(\mathbf{k}) + V_x(\mathbf{k}), \quad (\text{C4})$$

where

$$\begin{aligned} \varepsilon_0(\mathbf{k}) &= \frac{\hbar^2 k^2}{2m}, \\ V_x(\mathbf{k}) &= -\frac{1}{L^3} \sum_{\mathbf{k}'} \frac{4\pi e^2}{\epsilon |\mathbf{k} - \mathbf{k}'|^2} f(\varepsilon_{\mathbf{k}'}), \end{aligned} \quad (\text{C5})$$

and the Fermi momentum $k_F = (6\pi^2 n)^{1/3}$. The dimensionless distance

$$r_s a^* = \left(\frac{3}{4\pi n} \right)^{1/3}. \quad (\text{C6})$$

At $T = 0$, the exchange potential

$$\begin{aligned} V_x(\mathbf{k}) &= -\frac{1}{L^3} \sum_{\mathbf{k}' \leq k_F} \frac{4\pi e^2}{\epsilon |\mathbf{k} - \mathbf{k}'|^2} \\ &= -\int_{\mathbf{k}' \leq k_F} \frac{d^3 \mathbf{k}'}{(2\pi)^3} \frac{4\pi e^2}{\epsilon |\mathbf{k} - \mathbf{k}'|^2} \end{aligned}$$

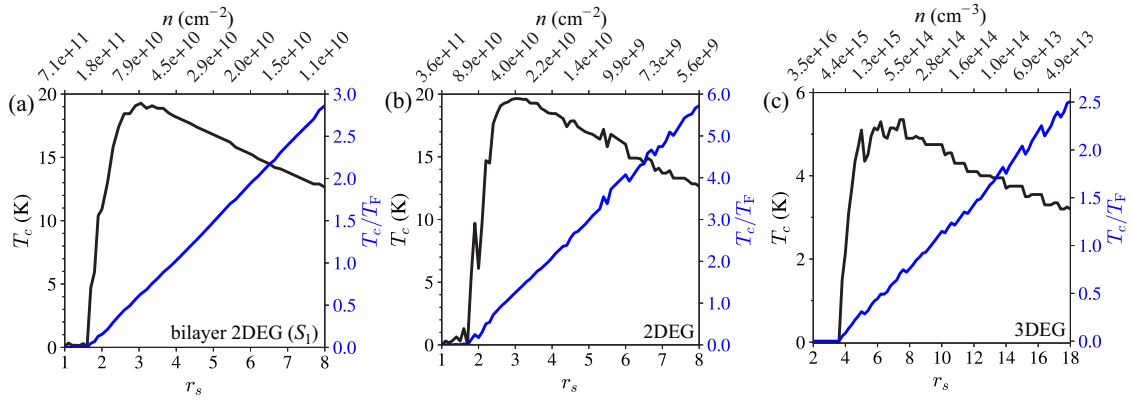


FIG. 20. T_c of the spin-polarized state, calculated by finite-temperature self-consistent HF. (a) For bilayer 2DEG, i.e., the S_1 phase in Sec. III A 2. Note that T_c of the S_1 phase is d independent. (b) For single 2DEG. (c) For single 3DEG.

$$\begin{aligned}
 &= -\frac{e^2 k_F}{\pi \epsilon} \int_{-1}^1 d \cos \theta \int_0^1 dx \frac{x^2}{x^2 + y^2 - 2xy \cos \theta} \\
 &= -\frac{2e^2 k_F}{\pi \epsilon} f_{3D} \left(\frac{k}{k_F} \right), \quad (C7)
 \end{aligned}$$

where $x = k'/k_F$, $y = k/k_F$, and

$$f_{3D}(x) = \frac{1}{2} + \frac{1-x^2}{4x} \ln \left| \frac{1+x}{1-x} \right|. \quad (C8)$$

At finite T , the exchange potential is evaluated numerically:

$$\begin{aligned}
 V_x(\mathbf{k}) &= -\int_{k' \leq k_F} \frac{d^3 \mathbf{k}'}{(2\pi)^3} \frac{4\pi e^2}{\epsilon |\mathbf{k} - \mathbf{k}'|^2} f(\epsilon_{\mathbf{k}'}) \\
 &= -\frac{e^2}{\pi \epsilon} \int_{-1}^1 dz \int_0^{k_F} dk' \frac{(k')^2}{(k')^2 + k^2 - 2k'kz} f(\epsilon_{\mathbf{k}'}). \quad (C9)
 \end{aligned}$$

T_c of 3DEG spin-polarized state, calculated by finite-temperature SCHF, is shown in Fig. 20(c).

- [1] T. Ando, A. B. Fowler, and F. Stern, *Rev. Mod. Phys.* **54**, 437 (1982).
- [2] S. Das Sarma and A. Pinczuk, *Perspectives in Quantum Hall Effects* (Wiley, Hoboken, NJ, 2008).
- [3] E. Wigner, *Phys. Rev.* **46**, 1002 (1934).
- [4] F. Bloch, *Z. Phys.* **57**, 545 (1929).
- [5] J. Bardeen, L. N. Cooper, and J. R. Schrieffer, *Phys. Rev.* **106**, 162 (1957).
- [6] J. Bardeen, L. N. Cooper, and J. R. Schrieffer, *Phys. Rev.* **108**, 1175 (1957).
- [7] L. V. Keldysh and Y. V. Kopaev, *Fiz. Tverd. Tela* **6**, 2791 (1965) [*Sov. Phys.-Solid State* **6**, 2219 (1965)].
- [8] D. Jérôme, T. M. Rice, and W. Kohn, *Phys. Rev.* **158**, 462 (1967).
- [9] L. V. Keldysh and A. N. Kozlov, *Zh. Eksp. Teor. Fiz.* **54**, 978 (1968) [*Sov. J. Exp. Theor. Phys.* **27**, 521 (1968)].
- [10] A. N. Kozlov and L. A. Maksimov, *Zh. Eksp. Teor. Fiz.* **48**, 1184 (1965) [*Sov. Phys.-JETP* **21**, 790 (1965)].
- [11] B. I. Halperin and T. M. Rice, *Rev. Mod. Phys.* **40**, 755 (1968).
- [12] J. Frenkel, *Phys. Rev.* **37**, 17 (1931).
- [13] G. H. Wannier, *Phys. Rev.* **52**, 191 (1937).
- [14] R. S. Knox, *Theory of Excitons* (Academic Press New York, 1963).
- [15] L. Du, X. Li, W. Lou, G. Sullivan, K. Chang, J. Kono, and R.-R. Du, *Nat. Commun.* **8**, 1971 (2017).
- [16] A. F. Croxall, K. Das Gupta, C. A. Nicoll, M. Thangaraj, H. E. Beere, I. Farrer, D. A. Ritchie, and M. Pepper, *Phys. Rev. Lett.* **101**, 246801 (2008).
- [17] K. Das Gupta, M. Thangaraj, A. Croxall, H. Beere, C. Nicoll, D. Ritchie, and M. Pepper, *J. Phys. E* **40**, 1693 (2008).
- [18] J. A. Seamons, D. R. Tibbetts, J. L. Reno, and M. P. Lilly, *Appl. Phys. Lett.* **90**, 052103 (2007).
- [19] Y. E. Lozovik and V. I. Yudson, *Pis'ma Zh. Eksp. Teor. Fiz.* **22**, 556 (1975) [*JETP Lett.* **22**, 11 (1975)].
- [20] S. I. Shevchenko, *Sov. J. Low Temp. Phys.* **2**, 4 (1976).
- [21] Y. Naveh and B. Laikhtman, *Phys. Rev. Lett.* **77**, 900 (1996).
- [22] S. Datta, M. R. Melloch, and R. L. Gunshor, *Phys. Rev. B* **32**, 2607 (1985).
- [23] X. Zhu, P. B. Littlewood, M. S. Hybertsen, and T. M. Rice, *Phys. Rev. Lett.* **74**, 1633 (1995).
- [24] P. B. Littlewood and X. Zhu, *Phys. Scr.* **T68**, 56 (1996).
- [25] L. Butov, *Solid State Commun.* **127**, 89 (2003).
- [26] P. X. Nguyen, L. Ma, R. Chaturvedi, K. Watanabe, T. Taniguchi, J. Shan, and K. F. Mak, [arXiv:2309.14940](https://arxiv.org/abs/2309.14940).
- [27] S. M. Girvin and A. H. MacDonald, in *Perspectives in Quantum Hall Effects* (Wiley, New York, 1996), Chap. 5, pp. 161–224.
- [28] J. P. Eisenstein, in *Perspectives in Quantum Hall Effects* (Wiley, New York, 1996), Chap. 2, pp. 37–70.
- [29] J. P. Eisenstein and A. H. MacDonald, *Nature (London)* **432**, 691 (2004).
- [30] J. Eisenstein, *Annu. Rev. Condens. Matter Phys.* **5**, 159 (2014).
- [31] M. Kellogg, J. P. Eisenstein, L. N. Pfeiffer, and K. W. West, *Phys. Rev. Lett.* **93**, 036801 (2004).

- [32] E. Tutuc, M. Shayegan, and D. A. Huse, *Phys. Rev. Lett.* **93**, 036802 (2004).
- [33] J. P. Eisenstein, *Science* **305**, 950 (2004).
- [34] J. I. A. Li, T. Taniguchi, K. Watanabe, J. Hone, and C. R. Dean, *Nat. Phys.* **13**, 751 (2017).
- [35] X. Liu, K. Watanabe, T. Taniguchi, B. I. Halperin, and P. Kim, *Nat. Phys.* **13**, 746 (2017).
- [36] Y. Zeng, Q. Shi, A. Okounkova, D. Sun, K. Watanabe, T. T., J. Hone, C. Dean, and J. Li, [arXiv:2306.16995](https://arxiv.org/abs/2306.16995).
- [37] X. Liu, J. I. A. Li, K. Watanabe, T. Taniguchi, J. Hone, B. I. Halperin, P. Kim, and C. R. Dean, *Science* **375**, 205 (2022).
- [38] M. M. Parish, The bcs-bec crossover, in *Quantum Gas Experiments* (Imperial College Press, 2014), Chap. 9, pp. 179–197.
- [39] M. Randeria and E. Taylor, *Annu. Rev. Condens. Matter Phys.* **5**, 209 (2014).
- [40] Q. Chen, J. Stajic, S. Tan, and K. Levin, *Phys. Rep.* **412**, 1 (2005).
- [41] T. Bourdel, L. Khaykovich, J. Cubizolles, J. Zhang, F. Chevy, M. Teichmann, L. Tarruell, S. J. J. M. F. Kokkelmans, and C. Salomon, *Phys. Rev. Lett.* **93**, 050401 (2004).
- [42] C. A. Regal, M. Greiner, and D. S. Jin, *Phys. Rev. Lett.* **92**, 040403 (2004).
- [43] M. Bartenstein, A. Altmeyer, S. Riedl, S. Jochim, C. Chin, J. H. Denschlag, and R. Grimm, *Phys. Rev. Lett.* **92**, 203201 (2004).
- [44] M. W. Zwierlein, C. A. Stan, C. H. Schunck, S. M. F. Raupach, A. J. Kerman, and W. Ketterle, *Phys. Rev. Lett.* **92**, 120403 (2004).
- [45] M. G. Ries, A. N. Wenz, G. Zürn, L. Bayha, I. Boettcher, D. Kedar, P. A. Murthy, M. Neidig, T. Lompe, and S. Jochim, *Phys. Rev. Lett.* **114**, 230401 (2015).
- [46] P. A. Murthy, M. Neidig, R. Klemt, L. Bayha, I. Boettcher, T. Enss, M. Holten, G. Zürn, P. M. Preiss, and S. Jochim, *Science* **359**, 452 (2018).
- [47] S. Rinott, K. B. Chashka, A. Ribak, E. D. L. Rienks, A. Taleb-Ibrahimi, P. L. Fevre, F. Bertran, M. Randeria, and A. Kanigel, *Sci. Adv.* **3**, e1602372 (2017).
- [48] Y. Nakagawa, Y. Kasahara, T. Nomoto, R. Arita, T. Nojima, and Y. Iwasa, *Science* **372**, 190 (2021).
- [49] L. Zhu, X. Liu, L. Li, X. Wan, R. Tao, Z. Xie, J. Feng, and C. Zeng, *Nat. Commun.* **14**, 1465 (2023).
- [50] G. W. Burg, N. Prasad, K. Kim, T. Taniguchi, K. Watanabe, A. H. MacDonald, L. F. Register, and E. Tutuc, *Phys. Rev. Lett.* **120**, 177702 (2018).
- [51] A. MacDonald, *Phys. B (Amsterdam)* **298**, 129 (2001).
- [52] H. A. Fertig, *Phys. Rev. B* **40**, 1087 (1989).
- [53] K. Yang, K. Moon, L. Belkhir, H. Mori, S. M. Girvin, A. H. MacDonald, L. Zheng, and D. Yoshioka, *Phys. Rev. B* **54**, 11644 (1996).
- [54] A. H. MacDonald, P. M. Platzman, and G. S. Boebinger, *Phys. Rev. Lett.* **65**, 775 (1990).
- [55] D. Yoshioka and A. H. MacDonald, *J. Phys. Soc. Jpn.* **59**, 4211 (1990).
- [56] Z. F. Ezawa and A. Iwazaki, *Phys. Rev. B* **47**, 7295 (1993).
- [57] K. Yang, K. Moon, L. Zheng, A. H. MacDonald, S. M. Girvin, D. Yoshioka, and S.-C. Zhang, *Phys. Rev. Lett.* **72**, 732 (1994).
- [58] K. Moon, H. Mori, K. Yang, S. M. Girvin, A. H. MacDonald, L. Zheng, D. Yoshioka, and S.-C. Zhang, *Phys. Rev. B* **51**, 5138 (1995).
- [59] O. Kyriienko, K. Wierschem, P. Sengupta, and I. A. Shelykh, *Europhys. Lett.* **109**, 57003 (2015).
- [60] A. Stern, S. Das Sarma, M. P. A. Fisher, and S. M. Girvin, *Phys. Rev. Lett.* **84**, 139 (2000).
- [61] L. Zheng, M. W. Ortalano, and S. Das Sarma, *Phys. Rev. B* **55**, 4506 (1997).
- [62] S. Das Sarma, M. W. Ortalano, and L. Zheng, *Phys. Rev. B* **58**, 7453 (1998).
- [63] X.-G. Wen and A. Zee, *Phys. Rev. Lett.* **69**, 1811 (1992).
- [64] T. Nakajima and H. Aoki, *Phys. Rev. B* **56**, R15549 (1997).
- [65] Y. N. Joglekar, A. V. Balatsky, and S. Das Sarma, *Phys. Rev. B* **74**, 233302 (2006).
- [66] S. M. Sze, *Physics of Semiconductor Devices* (Wiley, New York, 1981), p. 850.
- [67] C. B. Hanna, D. Haas, and J. C. Díaz-Vélez, *Phys. Rev. B* **61**, 13882 (2000).
- [68] Y.-P. Shim and A. H. MacDonald, *Phys. Rev. B* **79**, 235329 (2009).
- [69] P. López Ríos, A. Perali, R. J. Needs, and D. Neilson, *Phys. Rev. Lett.* **120**, 177701 (2018).
- [70] J. P. Eisenstein, L. N. Pfeiffer, and K. W. West, *Phys. Rev. Lett.* **123**, 066802 (2019).
- [71] N. E. Bonesteel, I. A. MacDonald, and C. Nayak, *Phys. Rev. Lett.* **77**, 3009 (1996).
- [72] T. Morinari, *Phys. Rev. B* **59**, 7320 (1999).
- [73] Y. B. Kim, C. Nayak, E. Demler, N. Read, and S. Das Sarma, *Phys. Rev. B* **63**, 205315 (2001).
- [74] G. Möller, S. H. Simon, and E. H. Rezayi, *Phys. Rev. B* **79**, 125106 (2009).
- [75] G. Wagner, D. X. Nguyen, S. H. Simon, and B. I. Halperin, *Phys. Rev. Lett.* **127**, 246803 (2021).
- [76] D. Vu and S. Das Sarma, *Phys. Rev. B* **108**, 235150 (2023).
- [77] L. Zheng, R. J. Radtke, and S. Das Sarma, *Phys. Rev. Lett.* **78**, 2453 (1997).
- [78] S. Das Sarma, S. Sachdev, and L. Zheng, *Phys. Rev. Lett.* **79**, 917 (1997).
- [79] S. Das Sarma, S. Sachdev, and L. Zheng, *Phys. Rev. B* **58**, 4672 (1998).
- [80] A. H. MacDonald, R. Rajaraman, and T. Jungwirth, *Phys. Rev. B* **60**, 8817 (1999).
- [81] K. Yang, *Phys. Rev. B* **60**, 15578 (1999).
- [82] E. Demler and S. Das Sarma, *Phys. Rev. Lett.* **82**, 3895 (1999).
- [83] J. Schliemann and A. H. MacDonald, *Phys. Rev. Lett.* **84**, 4437 (2000).
- [84] E. Demler, E. H. Kim, and S. Das Sarma, *Phys. Rev. B* **61**, R10567 (2000).
- [85] V. Pellegrini, A. Pinczuk, B. S. Dennis, A. S. Plaut, L. N. Pfeiffer, and K. W. West, *Phys. Rev. Lett.* **78**, 310 (1997).
- [86] V. Pellegrini, A. Pinczuk, B. S. Dennis, A. S. Plaut, L. N. Pfeiffer, and K. W. West, *Science* **281**, 799 (1998).
- [87] V. S. Khrapai, E. V. Deviatov, A. A. Shashkin, V. T. Dolgoplov, F. Hastreiter, A. Wixforth, K. L. Campman, and A. C. Gossard, *Phys. Rev. Lett.* **84**, 725 (2000).
- [88] D. Nandi, A. D. K. Finck, J. P. Eisenstein, L. N. Pfeiffer, and K. W. West, *Nature (London)* **488**, 481 (2012).

- [89] M. Kellogg, I. B. Spielman, J. P. Eisenstein, L. N. Pfeiffer, and K. W. West, *Phys. Rev. Lett.* **88**, 126804 (2002).
- [90] R. D. Wiersma, J. G. S. Lok, S. Kraus, W. Dietsche, K. von Klitzing, D. Schuh, M. Bichler, H.-P. Tranitz, and W. Wegscheider, *Phys. Rev. Lett.* **93**, 266805 (2004).
- [91] I. B. Spielman, J. P. Eisenstein, L. N. Pfeiffer, and K. W. West, *Phys. Rev. Lett.* **84**, 5808 (2000).
- [92] I. B. Spielman, J. P. Eisenstein, L. N. Pfeiffer, and K. W. West, *Phys. Rev. Lett.* **87**, 036803 (2001).
- [93] A. D. K. Finck, J. P. Eisenstein, L. N. Pfeiffer, and K. W. West, *Phys. Rev. Lett.* **106**, 236807 (2011).
- [94] L. Balents and L. Radzihovsky, *Phys. Rev. Lett.* **86**, 1825 (2001).
- [95] E. Rossi, A. S. Núñez, and A. H. MacDonald, *Phys. Rev. Lett.* **95**, 266804 (2005).
- [96] J. A. Seamons, C. P. Morath, J. L. Reno, and M. P. Lilly, *Phys. Rev. Lett.* **102**, 026804 (2009).
- [97] M. L. Davis, S. Parolo, C. Reichl, W. Dietsche, and W. Wegscheider, *Phys. Rev. Lett.* **131**, 156301 (2023).
- [98] S. Misra, N. C. Bishop, E. Tutuc, and M. Shayegan, *Phys. Rev. B* **77**, 161301(R) (2008).
- [99] J. P. Eisenstein, T. J. Gramila, L. N. Pfeiffer, and K. W. West, *Phys. Rev. B* **44**, 6511 (1991).
- [100] J. P. Eisenstein, L. N. Pfeiffer, and K. W. West, *Appl. Phys. Lett.* **58**, 1497 (1991).
- [101] Y. Kim, A. H. MacDonald, and M. J. Gilbert, *Phys. Rev. B* **85**, 165424 (2012).
- [102] S. Das Sarma and A. Madhukar, *Phys. Rev. B* **23**, 805 (1981).
- [103] S. Das Sarma and E. H. Hwang, *Phys. Rev. Lett.* **81**, 4216 (1998).
- [104] H. A. Fertig and S. Das Sarma, *Phys. Rev. Lett.* **65**, 1482 (1990).
- [105] T. Cookmeyer and S. Das Sarma, [arXiv:2312.10791](https://arxiv.org/abs/2312.10791).